Applied Mathematical Modelling 48 (2017) 451–475

Contents lists available at ScienceDirect

Applied Mathematical Modelling

journal homepage: www.elsevier.com/locate/apm

Dynamic analysis of short and long journal bearings in laminar and turbulent regimes, application in critical shaft stiffness determination

Farzad Hemmati [a,*], Mohammad Miraskari [a], Mohamed S. Gadala [b]

[a] Mechanical Engineering Department, University of British Columbia, 2054-6250 Applied Science Lane, Vancouver, BC V6T 1Z4, Canada
[b] Mechanical Engineering Department, Abu Dhabi University, Abu Dhabi, United Arab Emirates

ARTICLE INFO

Article history:
Received 8 November 2016
Revised 24 March 2017
Accepted 5 April 2017
Available online 13 April 2017

Keywords:
Linear and nonlinear stability analysis
Hopf bifurcation theory
Short and long journal bearings
Constantinescu's and Ng–Pan–Elrod turbulent models
Critical shaft stiffness

ABSTRACT

Linear and non-linear stability of a flexible rotor-bearing system supported on short and long journal bearings is studied for both laminar and turbulent operating conditions. The turbulent pressure distribution and forces are calculated analytically from the modified Reynolds equation based on two turbulent models; Constantinescu's and Ng–Pan–Elrod. Hopf bifurcation theory was utilized to estimate the local stability of periodic solutions near bifurcating operating points. The shaft stiffness was found to play an important role in bifurcating regions on the stable boundaries. It was found that for shafts supported on short journal bearings with shaft stiffness above a critical value, the dangerous subcritical region can be eliminated from a range of operating conditions with high static load. The results presented have been verified by published results in the open literature.

1. Introduction

The demand for high pressure injection of natural gas in underground has led to the design of multistage compressors. In 1970s many of such compressors were suffering from violent sub-synchronous whirl [1], a form of self-excited instability. In turbo-machinery, instabilities are characterized by whirling of the rotor bearing systems at frequencies other than the rotating frequency of the shaft. While large amplitudes of sub-synchronous vibration do not occur frequently, they can appear at certain operating conditions and can lead to high amplitude and destructive vibrations. If the operating speed of rotors exceeds a threshold speed known as "threshold speed of instability", the rotor-bearing system becomes unstable in oil whirl/whip which is characterized by sub-synchronous whirling [2]. Linearized stiffness and damping coefficients (dynamic coefficients) are used as basis for stability analysis of the rotor bearing systems. In the linearized analysis, bearing dynamic coefficients are evaluated at the equilibrium position of the journal.

While the load–displacement curve of a journal bearing is evidently nonlinear, the bearing behavior and stability can be characterized by means of linear dynamic coefficients if certain conditions are met. It is known that the "local" stability of a non-linear system and its linearized counterpart are essentially the same even though their stability type could be different. By local, one means that the current operating condition is close enough to an operating equilibrium point, a condition that is also vital for validity of utilizing linearized bearing coefficients to represent the journal force in rotor-bearing analysis. Choy et al. [3] calculated nonlinear bearing stiffness coefficients and showed that for displacements sufficiently far away from the equilibrium position, oil film forces will exhibit nonlinearities. Andres and Santiago [4] experimentally determined

* Corresponding author.
E-mail addresses: farhemmati@gmail.com (F. Hemmati), m.miraskari@alumni.ubc.ca (M. Miraskari), gadala@mech.ubc.ca (M.S. Gadala).

http://dx.doi.org/10.1016/j.apm.2017.04.013
0307-904X/

Nomenclature

L	bearing length
M	reduced mass of the rotor
C	radial clearance (m)
R	journal radius (m)
ε	eccentricity ratio
O	center of bearing chamber
O_j	center of the journal inside the chamber
g	gravitational constant (m/s^2)
ω	shaft rotating speed (rad/s)
$\bar{\omega}$	dimensionless shaft rotating speed ($\omega\sqrt{M/K_s}$)
$\bar{\omega}_s$	critical speed of the shaft
ω_w	whirl rotating speed (rad/s)
k_θ	circumferential turbulent coefficient
k_z	longitudinal turbulent coefficient
ρ	fluid film density (kg/m^3)
W	load per bearing ($\frac{Mg}{2}$)
$\bar{\Gamma}$	stability parameter ($\frac{C}{W}M\omega_s^2$)
$\bar{X}_i$	dimensionless coordinate in horizontal and vertical directions ($\frac{X_1}{C}$)
$\bar{K}_{ij}$	Cartesian-coordinate dimensionless stiffness coefficients $(\pi(C/R)^3/\mu\omega L)\,K_{ij}$
S_z	non-dimensional shaft stiffness coefficient, $(\frac{C}{W})K_s$
$\bar{F}_{r,t}$	non-dimensional forces, $F_{r,t}(\frac{\pi C^2}{\mu\omega LR^3})$
F_R	radial fluid force (N)
F_T	tangential fluid force (N)
F_x	radial fluid force in x direction (N)
F_y	radial fluid force in y direction (N)
F_x^t	total force on bearing in x direction (N)
F_y^t	total force on bearing in y direction (N)
S	Sommerfeld number ($\frac{\mu\omega LR^3}{\pi WC^2}$)
K_s	shaft stiffness
Ω	whirl frequency ratio
$\overline{Re}$	mean Reynolds number ($\frac{\rho R\omega C}{\mu}$)
Re^*	local Reynolds number ($\frac{\rho R\omega h}{\mu}$)
μ	fluid film (lubricant) viscosity (Pa s)
$\bar{k}_{ij}$	polar dimensionless stiffness coefficients $(\pi(C/R)^3/\mu\omega L)\,k_{ij}$
$\bar{c}_{ij}$	polar dimensionless damping coefficients $(\pi(C/R)^3/\mu L)\,c_{ij}$
θ	circumferential coordinate
φ	attitude angle
h	oil film thickness, $C(1+\varepsilon\cos(\theta))$
P	oil film pressure (Pa)
$\bar{P}$	dimensionless oil film pressure $((\frac{C}{D})^2\frac{8\pi}{\mu\omega})$
a_i, $\hat{a}_i$	turbulent constants
$\bar{C}_{ij}$	Cartesian-coordinate dimensionless damping coefficients $(\pi(C/R)^3/\mu L)\,C_{ij}$

the dynamic coefficients under high dynamic loads with large orbital motion of up to 50% of the bearing clearance. Their results are in good agreement with analytical linearized coefficients. Meruane and Pascual [5] estimated the linear and non-linear bearing coefficients under large orbital motion and even during oil whirl. They showed that the linearized analytical coefficients agree reasonably with linear coefficients estimated numerically considering a nonlinear model and under large orbital motion. Small variation between the linear and nonlinear model were reported provided that the operating speed is kept below the instability threshold speed. Muzakkir et al. [6] concluded, based on experimental results, that high viscosity lubricants for heavily loaded slow-speed journal bearings, in laminar regime flow, would improve bearing stability; however, no stability boundary region were provided. Lahmar et al. and Singh et al. [7,8] provided pressure distribution and bearing coefficients for thrust and compliant journal bearings under laminar flow assumption and no discussion were provided at high velocities were fluid film behaves turbulent.

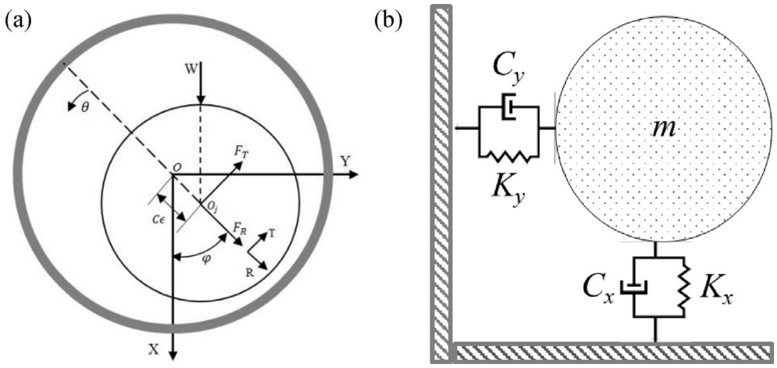

Fig. 1. (a) Schematic of a journal bearing, and (b) journal bearings fluid film model using linear stiffness and damping coefficients.

All of the abovementioned papers were based on the declaration that fluid-film flow remains laminar. Due to the high demand of large bearings running at high rotating speeds and also using low kinematic viscosity of lubrications, the fluid film region is turbulence. Instability analysis of large bearings cannot be accurately achieved when using classical lubrication theory (i.e. Reynolds equation). The reason for this is mostly because of two underlying assumptions to derive Reynolds equation: the assumption of laminar flow and constant viscosity in the oil film [9]. To correctly predict the bearing performance required for precise identification of instability phenomenon, the flow regime (being laminar or turbulent) needs to be taken into account. Therefore, it is important to determine the turbulent effects on the dynamic fluid forces and operating stability margin of journal bearings for reliable operation of rotor-bearing systems. Research dealing with the effect of turbulence on performance of fluid-film journal bearings has been primarily limited to steady-state, with the exception of a series of notable contributions by Hashimoto et al. [10,11] and Wang and Khonsari [12] who investigated dynamic effects using analytical methods for short bearing theory. However, their simplifying assumptions added to the Ng−Pan−Elrod model in order to analytically derive the short bearing forces leads to high errors at large eccentricity ratios and high Reynolds numbers. Chang-Jian and Chen [13,14] investigated the dynamics of a flexible rotor bearing system supported by two turbulent journal bearings; however, their treatment in deriving the analytical turbulent force components leads into erroneous results.

The purpose of this paper is first to derive an analytical expression to accurately estimate the turbulent short and long bearing forces and turbulent dynamic coefficients for the whole range of operating conditions. These coefficients and forces are then used as basis of linear and nonlinear stability analysis of a flexible rotor-bearing system. In this paper the authors describe the short and long bearing theory for the dynamic characteristic problems of turbulent fluid-film journal bearings on a flexible shaft. The dynamic oil film forces are analytically obtained utilizing Constantinescu and Ng–Pan–Elrod turbulent models under the short and long bearing assumptions with Gümbel's boundary condition. The closed form expressions for eight spring and damping coefficients are derived by linearizing the oil film forces around the steady-state equilibrium position of the journal center, and the whirl onset velocities are determined by the linear stability criterion. For nonlinear stability analysis, Hopf bifurcation theory is used to find the local stability of periodic solutions near bifurcating operating points. Results show minor difference between laminar and turbulent stability boundaries at high Sommerfeld numbers, while significant reduction in the size of the stable region was observed at low Sommerfeld numbers. This reduction in the size of stable region is further increased at high Reynolds numbers. The shaft stiffness was found to play an important role in bifurcating regions on the stable boundaries. The results predicted based on the flexible rotor model have been verified by results provided by Wang and Khonsari [15]. The critical shaft stiffness was introduced for the first time, at the point of transferring two bifurcation regions to three bifurcation regions. This critical shaft stiffness was shown to be a strong function of Reynolds at low Reynolds numbers for both short and long bearing supported shafts. The stability envelope in subcritical region of operation was calculated based on the Hopf bifurcation theory and was shown to reduce in size as the flow regime is transitioned from laminar to turbulent.

2. Governing equations and turbulent lubrication models

Fig. 1(a) shows a schematic of a journal bearing inside the bearing clearance. A simple rotor-bearing system can be represented as a concentrated mass supported on journal bearings modeled as direct and cross coupled spring and dampers as shown in Fig. 1(b) (cross coupled coefficients are not shown).

According to Fig. 1(a), under static equilibrium, the weight of the rotor and journal is in balance with the bearing force such that $\vec{F}+\vec{W}=0$ and hence relative to the static equilibrium state, the x and y components of the dynamic deviation of bearing force upon the rotor can be expressed as follows:

$$F_x + W_x = F_x^t = \frac{\partial F_x^t}{\partial x}x + \frac{\partial F_x^t}{\partial \dot{x}}\dot{x} + \frac{\partial F_x^t}{\partial y}y + \frac{\partial F_x^t}{\partial \dot{y}}\dot{y} + \text{(higher order terms)}$$

Table 1
Turbulent constants of Constantinescu and Ng–Pan–Elrod model.

Constants	Turbulence methods	
	Constantinescu model	Ng–Pan–Elrod model
a_1	0.0198	0.0044
a_2	0.741	0.96
$\hat{a}_1$	0.026	0.0136
$\hat{a}_2$	0.8265	0.9

$$F_y + W_y = F_y^t = \frac{\partial F_y^t}{\partial x}x + \frac{\partial F_y^t}{\partial \dot{x}}\dot{x} + \frac{\partial F_y^t}{\partial y}y + \frac{\partial F_y^t}{\partial \dot{y}}\dot{y} + (\text{higher order terms}). \tag{1}$$

It is convenient to write Eq. (1) in the following matrix form:

$$\begin{Bmatrix} F_x^t \\ F_y^t \end{Bmatrix} = -\begin{bmatrix} k_{xx} & k_{xy} \\ k_{yx} & k_{yy} \end{bmatrix}\begin{Bmatrix} x \\ y \end{Bmatrix} - \begin{bmatrix} c_{xx} & c_{xy} \\ c_{yx} & c_{yy} \end{bmatrix}\begin{Bmatrix} \dot{x} \\ \dot{y} \end{Bmatrix}, \tag{2}$$

where $k_{ij} \equiv -(\partial F_i^t/\partial x_j)$ and $c_{ij} \equiv -(\partial F_i^t/\partial \dot{x}_j)$ are the eight bearing stiffness and damping coefficients as proposed by Lund [16].

The state of the flow in fluid-film journal bearings can be judged by its Reynolds number. Turbulence comes into an effect at mean Reynolds number ($\overline{Re}$) of approximately 2000 and higher [17]. For unsteady, incompressible turbulent flows in the oil film journal bearings as shown in Fig. 1, the Reynolds equation in the cylindrical coordinate system can be written as:

$$\frac{1}{R^2}\frac{\partial}{\partial \theta}\left(\frac{h^3}{k_\theta \mu}\frac{\partial P}{\partial \theta}\right) + \frac{\partial}{\partial z}\left(\frac{h^3}{k_z \mu}\frac{\partial P}{\partial z}\right) = \frac{\omega}{2}\frac{\partial h}{\partial \theta} + \frac{\partial h}{\partial t}, \tag{3}$$

where h is the fluid film thickness and k_θ and k_z are the turbulence coefficients in circumferential and longitudinal directions, respectively. In this paper two turbulence methods are employed. First is Constantinescu's model based on the Prandtl mixing length hypothesis [18,19]; second, is the Ng–Pan–Elrod model based on eddy viscosity [18,20]. Frene et al. [21] mentioned Constantinescu's approach is valid for $2000 \le \overline{Re} \le 10^5$. Durany et al. [22] stated that Constantinescu's approach is effective for $1000 \le \overline{Re} \le 10^5$. Furthermore, Constantinescu mentioned his results are in good agreement with Fuller's experiment for $2000 \le \overline{Re} \le 5 \times 10^4$ in his paper [19]. The turbulence coefficients along with their constants are presented in Eq. (5) and Table 1,

$$h = C(1 + \epsilon \mathrm{Cos}(\theta)), \tag{4}$$

$$\begin{cases} k_z = 12 + a_1 (Re^*)^{a_2} \\ k_\theta = 12 + \hat{a}_1 (Re^*)^{\hat{a}_2} \end{cases}, \tag{5}$$

where $Re^* = \frac{\rho R \omega h}{\mu} = \frac{\rho R \omega C(1+\epsilon \mathrm{Cos}(\theta))}{\mu}$ is the local Reynolds number and varies with θ. The local Reynolds number adds an extra nonlinearity term to the classical Reynolds equation which makes it impossible to derive an exact analytical expression for short and long bearing approximations. In Section 3, assumptions to analytically derive accurate fluid-film forces for short and long bearing approximations are explained in detail.

It has to be mentioned that, the turbulence coefficients should be considered in the Reynolds equation when the mean Reynolds value ($\overline{Re}$) is above 2000. The variation of k_θ and k_z with Re^* is shown in Fig. 2. As it can be seen from Fig. 2, the discrepancy between Constantinescu's approach and Ng–Pan–Elrod model increases by increasing the local Reynolds number. This reason for the difference lies in Constantinescu's turbulent model, where buffer zone is left untreated and non-planar flows have not been carefully modeled. Also accurate measurement of the mixing length constant for fluid-film bearings with small clearances is a big challenge in Constantinescu's model while most of the mentioned problems are addressed in Ng–Pan–Elrod turbulent formulation [18].

3. Analytical derivation of dynamic turbulent fluid-film forces

3.1. Turbulent short bearing theory formulation

From Eqs. (3) and (4), and considering $\dot{\theta} = -\dot{\varphi}$ [23], turbulent Reynolds equation may be written as:

$$\frac{1}{R^2}\frac{\partial}{\partial \theta}\left(\frac{h^3}{k_\theta \mu}\frac{\partial P}{\partial \theta}\right) + \frac{\partial}{\partial z}\left(\frac{h^3}{k_z \mu}\frac{\partial P}{\partial z}\right) = 0.5C((2\dot{\varphi} - \omega)\epsilon \mathrm{Sin}(\theta) + 2\dot{\epsilon}\mathrm{Cos}(\theta)). \tag{6}$$

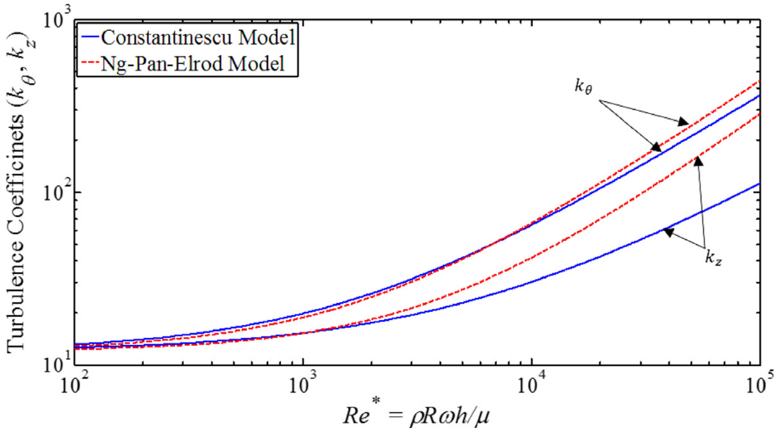

Fig. 2. Variation of turbulence constants k_θ and k_z with local Reynolds number.

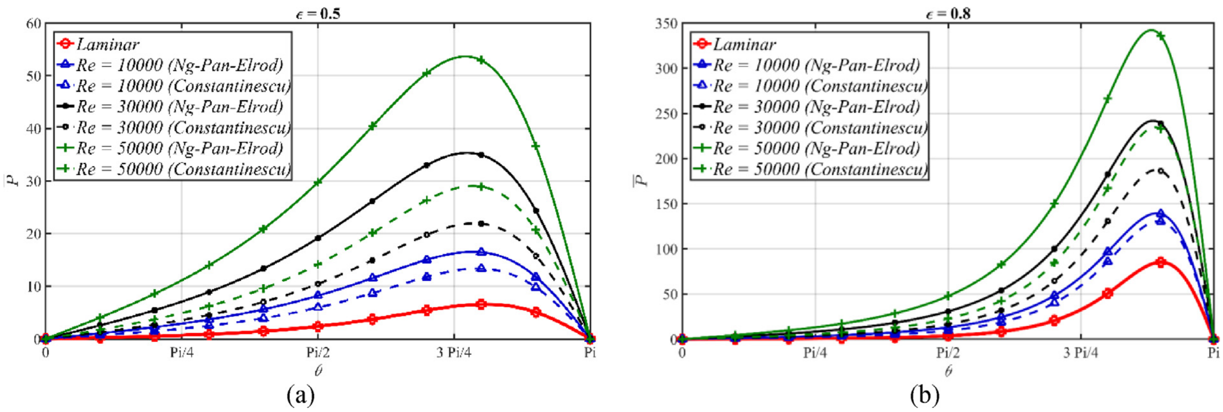

Fig. 3. The comparison of analytically obtained non-dimensional pressure distributions at mid-span of a short journal bearing with $L/D=0.5$ for laminar and turbulent flows at (a) $\varepsilon=0.5$, and (b) $\varepsilon=0.8$.

By short bearing approximation $(L/D) \le 0.5$, it may be assumed axial pressure flow dominates circumferential pressure flow [24]. Since the first term in Reynolds' equation disappears, updated turbulence Reynolds' equation for turbulent short bearing theory can be written as:

$$\frac{\partial^2 P}{\partial z^2} = \frac{k_z \mu C}{2h^3}((2\dot{\varphi} - \omega)\epsilon \mathrm{Sin}(\theta) + 2\dot{\epsilon}\mathrm{Cos}(\theta)) \tag{7}$$

By applying the boundary conditions $(z = \pm\frac{L}{2} \rightarrow\ P = 0)$, turbulence short bearing pressure may be written as:

$$P = \frac{k_z \mu C}{16h^3}((2\dot{\varphi} - \omega)\epsilon \mathrm{Sin}(\theta) + 2\dot{\epsilon}\mathrm{Cos}(\theta))\left(4z^2 - L^2\right). \tag{8}$$

The comparison of non-dimensional static pressure distribution at the journal mid-span $(z=0)$ for laminar and turbulent models at two eccentricity ratios are shown in Fig. 3 from 0 to π, since Gümbel boundary condition is used to produce bearing forces. where the dimensionless pressure $\bar{P} = P\ 8\pi\,(C/D)^2/\mu\omega$. The corresponding pressure distributions are evaluated for two different cases. First for relatively low eccentricity ratio of $\varepsilon=0.5$ and high eccentricity ratio of $\varepsilon=0.8$, as shown in Fig. 3(a) and (b), respectively. Results indicate that, as Reynolds number increases at higher loading conditions, the predicted pressure distributions of the modified Reynolds equation deviates significantly from the pressure as predicted by classical Reynolds equation (Laminar bearing theory). As it is shown in Fig. 3(a) and (b), Ng–Pan–Elrod fluid film turbulence model is more conservative compare to Constantinescu's model due to its higher evaluation of fluid-film pressure. The resulting fluid film turbulent forces acting on journal bearing in radial and tangential directions (rotating system of coordinates) can be found through integration of Eq. (8) over the area of journal bearing considering Gümbel (π film) boundary condition,

$$F_R = \int_0^{\pi} R d\theta \int_{-\frac{L}{2}}^{\frac{L}{2}} P\mathrm{Cos}(\theta) dz$$

$$F_t = \int_0^{\pi} R d\theta \int_{-\frac{L}{2}}^{\frac{L}{2}} P \mathrm{Sin}(\theta) dz. \tag{9}$$

By substituting Eq. (8) into Eq. (9), force components in polar coordinates may be derived as follow:

$$\begin{aligned} F_R &= -\frac{L^3 \mu R C}{24} \int_0^{\pi} \frac{k_z}{h^3} ((2\dot{\varphi} - \omega)\epsilon \mathrm{Sin}(\theta) + 2\dot{\epsilon}\mathrm{Cos}(\theta))\mathrm{Cos}(\theta) d\theta \\ F_t &= -\frac{L^3 \mu R C}{24} \int_0^{\pi} \frac{k_z}{h^3} ((2\dot{\varphi} - \omega)\epsilon \mathrm{Sin}(\theta) + 2\dot{\epsilon}\mathrm{Cos}(\theta))\mathrm{Sin}(\theta) d\theta. \end{aligned} \tag{10}$$

By substituting the turbulence coefficients from Eq. (5) in Eq. (10), and expanding the terms into laminar and turbulent parts, the following equation may be derived:

$$\begin{aligned} F_R &= -\frac{L^3 \mu R}{24 C^2} \left(\begin{aligned} &\int_0^{\pi} \frac{12 \mathrm{Cos}(\theta)}{(1+\epsilon \mathrm{Cos}(\theta))^3} ((2\dot{\varphi} - \omega)\epsilon \mathrm{Sin}(\theta) + 2\dot{\epsilon}\mathrm{Cos}(\theta)) d\theta \\ &- \int_0^{\pi} \frac{a_1 \left(\overline{Re}(1+\epsilon \mathrm{Cos}(\theta))\right)^{a_2} \mathrm{Cos}(\theta)}{(1+\epsilon \mathrm{Cos}(\theta))^3} ((2\dot{\varphi} - \omega)\epsilon \mathrm{Sin}(\theta) + 2\dot{\epsilon}\mathrm{Cos}(\theta)) d\theta \end{aligned} \right) \\ F_t &= -\frac{L^3 \mu R}{24 C^2} \left(\begin{aligned} &\int_0^{\pi} \frac{12 \mathrm{Sin}(\theta)}{(1+\epsilon \mathrm{Cos}(\theta))^3} ((2\dot{\varphi} - \omega)\epsilon \mathrm{Sin}(\theta) + 2\dot{\epsilon}\mathrm{Cos}(\theta)) d\theta \\ &- \int_0^{\pi} \frac{a_1 \left(\overline{Re}(1+\epsilon \mathrm{Cos}(\theta))\right)^{a_2} \mathrm{Sin}(\theta)}{(1+\epsilon \mathrm{Cos}(\theta))^3} ((2\dot{\varphi} - \omega)\epsilon \mathrm{Sin}(\theta) + 2\dot{\epsilon}\mathrm{Cos}(\theta)) d\theta \end{aligned} \right), \end{aligned} \tag{11}$$

where $\overline{Re} = \frac{\rho R \omega C}{\mu}$ is defined as the mean Reynolds number. Therefore, the above equations can be simplified as,

$$\begin{aligned} F_R &= -\frac{L^3 \mu R}{24 C^2} \left\{ \left((\omega - 2\dot{\varphi}) \frac{24\epsilon^2}{\left(1-\epsilon^2\right)^2} + \frac{12\pi \left(1+2\epsilon^2\right)\dot{\epsilon}}{\left(1-\epsilon^2\right)^{5/2}} \right) \right. \\ &\left. + a_1 \left(\overline{Re}\right)^{a_2} \left(\begin{aligned} &(\omega - 2\dot{\varphi}) \frac{(1+\epsilon)^{a_2-2}(1-(a_2-2)\epsilon) - (1-\epsilon)^{a_2-2}(1+(a_2-2)\epsilon)}{(a_2-2)(a_2-1)\epsilon} \\ &+ 2\dot{\epsilon} \int_0^{\pi} \frac{\mathrm{Cos}(\theta)^2}{(1+\epsilon \mathrm{Cos}(\theta))^{3-a_2}} d\theta \end{aligned} \right) \right\} \\ F_t &= \frac{L^3 \mu R}{24 C^2} \left\{ \left((\omega - 2\dot{\varphi}) \frac{6\pi\epsilon}{\left(1-\epsilon^2\right)^{3/2}} + \frac{48\epsilon\dot{\epsilon}}{\left(1-\epsilon^2\right)^2} \right) \right. \\ &\left. + a_1 \left(\overline{Re}\right)^{a_2} \left(\begin{aligned} &(\omega - 2\dot{\varphi})\epsilon \int_0^{\pi} \frac{\mathrm{Sin}(\theta)^2}{(1+\epsilon \mathrm{Cos}(\theta))^{3-a_2}} d\theta \\ &- 2\dot{\epsilon} \frac{(1+\epsilon)^{a_2-2}((a_2-2)\epsilon - 1) + (1-\epsilon)^{a_2-2}((a_2-2)\epsilon + 1)}{(a_2-2)(a_2-1)\epsilon^2} \end{aligned} \right) \right\}. \end{aligned} \tag{12}$$

Since there are no explicit solutions for $\int_0^{\pi} \frac{(1+\epsilon \mathrm{Cos}(\theta))^{a_2} \mathrm{Sin}(\theta)^2}{(1+\epsilon \mathrm{Cos}(\theta))^3} d\theta)$ and $\int_0^{\pi} \frac{(1+\epsilon \mathrm{Cos}(\theta))^{a_2} \mathrm{Cos}(\theta)^2}{(1+\epsilon \mathrm{Cos}(\theta))^3} d\theta$, these integrations can be accurately approximated by the following expressions:

$$\begin{aligned} \int_0^{\pi} \frac{\mathrm{Cos}(\theta)^2}{(1+\epsilon \mathrm{Cos}(\theta))^{3-a_2}} d\theta &\approx \int_0^{\pi} \frac{(1+a_3\epsilon \mathrm{Cos}(\theta))\mathrm{Cos}(\theta)^2}{(1+\epsilon \mathrm{Cos}(\theta))^3} d\theta = \pi \left(\frac{a_3}{\epsilon^2} \frac{2\epsilon^4 + \epsilon^2 - a_3\left(6\epsilon^4 - 5\epsilon^2 + 2\right)}{2\epsilon^2\left(1-\epsilon^2\right)^{5/2}} \right) \\ \int_0^{\pi} \frac{\mathrm{Sin}(\theta)^2}{(1+\epsilon \mathrm{Cos}(\theta))^{3-a_2}} d\theta &\approx \int_0^{\pi} \frac{(1+a_4\epsilon \mathrm{Cos}(\theta))\mathrm{Sin}(\theta)^2}{(1+\epsilon \mathrm{Cos}(\theta))^3} d\theta = -\pi \frac{2a_4\left(1-\epsilon^2\right)^{3/2} - \epsilon^2 + a_4\left(3\epsilon^2 - 2\right)}{2\epsilon^2\left(1-\epsilon^2\right)^{3/2}}, \end{aligned} \tag{13}$$

where a_3, and a_4 are constants which can be found through optimization and curve fitting to $\int_0^{\pi} \frac{\mathrm{Cos}(\theta)^2}{(1+\epsilon \mathrm{Cos}(\theta))^{3-a_2}} d\theta$ and $\int_0^{\pi} \frac{\mathrm{Sin}(\theta)^2}{(1+\epsilon \mathrm{Cos}(\theta))^{3-a_2}} d\theta$, respectively. Constants a_3, and a_4 for Constantinescu's model are 0.9481 and 0.9589 and for Ng–Pan–Elrod model are found to be 0.9945 and 0.9747, respectively. Thus, the complete form of analytical turbulence forces for short bearing theory can be written as:

$$F_R = -\frac{L^3\mu R}{24C^2}\left\{\begin{array}{l}\left((\omega-2\dot{\varphi})\dfrac{24\epsilon^2}{\left(1-\epsilon^2\right)^2}+\dfrac{12\pi\left(1+2\epsilon^2\right)\dot{\epsilon}}{\left(1-\epsilon^2\right)^{5/2}}\right)\\ +\ a_1\left(\overline{Re}\right)^{a_2}\left((\omega-2\dot{\varphi})\dfrac{(1+\epsilon)^{a_2-2}(1-(a_2-2)\epsilon)-(1-\epsilon)^{a_2-2}(1+(a_2-2)\epsilon)}{(a_2-2)(a_2-1)\epsilon}\right.\\ \left.+\ (\pi\dot{\epsilon})\dfrac{2a_3\left(1-\epsilon^2\right)^{5/2}+2\epsilon^4+\epsilon^2-a_3\left(6\epsilon^4-5\epsilon^2+2\right)}{\epsilon^2\left(1-\epsilon^2\right)^{5/2}}\right)\end{array}\right\}$$

$$F_t = \frac{L^3\mu R}{24C^2}\left\{\begin{array}{l}\left((\omega-2\dot{\varphi})\dfrac{6\pi\epsilon}{\left(1-\epsilon^2\right)^{3/2}}+\dfrac{48\epsilon\dot{\epsilon}}{\left(1-\epsilon^2\right)^2}\right)\\ -\ a_1\left(\overline{Re}\right)^{a_2}\left(\pi(\omega-2\dot{\varphi})\dfrac{2a_4\left(1-\epsilon^2\right)^{3/2}-\epsilon^2+a_4\left(3\epsilon^2-2\right)}{2\epsilon\left(1-\epsilon^2\right)^{3/2}}\right.\\ \left.+\ 2\dot{\epsilon}\dfrac{(1+\epsilon)^{a_2-2}((a_2-2)\epsilon-1)+(1-\epsilon)^{a_2-2}((a_2-2)\epsilon+1)}{(a_2-2)(a_2-1)\epsilon^2}\right)\end{array}\right\}. \tag{14}$$

Having the force components in R and T directions by means of Eq. (14), the non-dimensional bearing stiffness and damping coefficients in R–T coordinate system are calculated as follows [12]:

$$\bar{k}_{ij} = \left(\pi (C/R)^3/\mu\omega L\right)\begin{pmatrix}-\dfrac{\partial F_R}{C\partial\epsilon} & -\dfrac{\partial F_R}{C\epsilon\partial\varphi}+\dfrac{F_T}{C\epsilon}\\ -\dfrac{\partial F_T}{C\partial\epsilon} & -\dfrac{\partial F_T}{C\epsilon\partial\varphi}-\dfrac{F_R}{C\epsilon}\end{pmatrix}$$

$$\bar{c}_{ij} = \left(\pi (C/R)^3/\mu L\right)\begin{pmatrix}-\dfrac{\partial F_R}{C\partial\dot{\epsilon}} & -\dfrac{\partial F_R}{C\epsilon\partial\dot{\varphi}}\\ -\dfrac{\partial F_T}{C\partial\dot{\epsilon}} & -\dfrac{\partial F_T}{C\epsilon\partial\dot{\varphi}}\end{pmatrix}. \tag{15}$$

It should be noted that journal bearing forces in a polar coordinate system are not functions of the attitude angle of the journal position; hence, $\frac{\partial F_R}{\partial\varphi} = \frac{\partial F_T}{\partial\varphi} = 0$. The non-dimensional form of turbulent stiffness and damping coefficients in polar coordinate system are tabulated in Table A1 (Appendix A). Having calculated the coefficients in the R–T (rotating) coordinate system, a simple coordinate transformation with angle of rotation being the journal bearing attitude angle φ, will yield the coefficients in X–Y (stationary) coordinate system. Having the confidents in stationary coordinate system will help to validate turbulent coefficients experimentally for future purposes,

$$M = \begin{pmatrix}\cos\varphi & -\sin\varphi\\ \sin\varphi & \cos\varphi\end{pmatrix}, \bar{K} = M\bar{k}M^T, \bar{C} = M\bar{c}M^T, \tag{16}$$

where M is the transformation matrix, $\bar{K}$ and $\bar{C}$ are the non-dimensional stiffness and damping coefficients in Cartesian (stationary) coordinate system, respectively. The dimensionless analytically calculated values for stiffness and damping of a short journal bearing coefficients in both laminar and turbulent regimes at different Reynolds numbers for a length to diameter ratio of $\frac{L}{D} = 0.5$ are plotted against their calculated Sommerfeld number ($S = \frac{\mu\omega LR^3}{\pi WC^2}$) and are shown in Fig. 4 and Fig. 5, respectively.

The Reynolds dependence of the dynamic stiffness coefficients in turbulent flow can be observed in Fig. 4. Although variation of the direct stiffness coefficient in y direction by increasing the Reynolds number is very small, the general trend for direct stiffness coefficient indicates that as the Reynolds number increases, the stiffness decreases for almost the whole range of Sommerfeld-loading conditions, Fig. 4(d). By comparing the results of direct turbulent stiffnesses for a fixed Reynolds number based on the two examined turbulent models, one can see that stiffness predictions based on Constantinescue's model (dashed lines) are higher than those predicted by the Ng–Pan–Elrod model (solid lines). The same trend, however, does not hold for the case of cross-coupled coefficients where trend-lines of dynamic stiffness cross each other at moderate Sommerfeld numbers and do not hold a consistent trend compared to the direct stiffness coefficients Fig. 4(b) and (c). The coefficients move to the top and left (higher values and lower Sommerfeld number) by increasing $\overline{Re}$. In both cases ($\bar{K}_{xy}$ and $abs(\bar{K}_{yx})$), at low Sommerfeld numbers, the stiffness predictions of Constantinescue's model remain higher compared to those of the Ng–Pan–Elrod model while this trend switches at high Sommerfeld values. Similarly, the higher calculated values of laminar stiffness at low Sommerfeld numbers will change to lower predictions at high Sommerfeld numbers compared to the turbulent values.

At high Sommerfeld numbers (moderate to low loading) the turbulent cross-coupled stiffness coefficients are generally higher compared to laminar stiffness coefficients and this suggests that a shaft supported on turbulent bearings could potentially be more stable at low loading which itself is the range where system is more susceptible to oil-whirl instability;

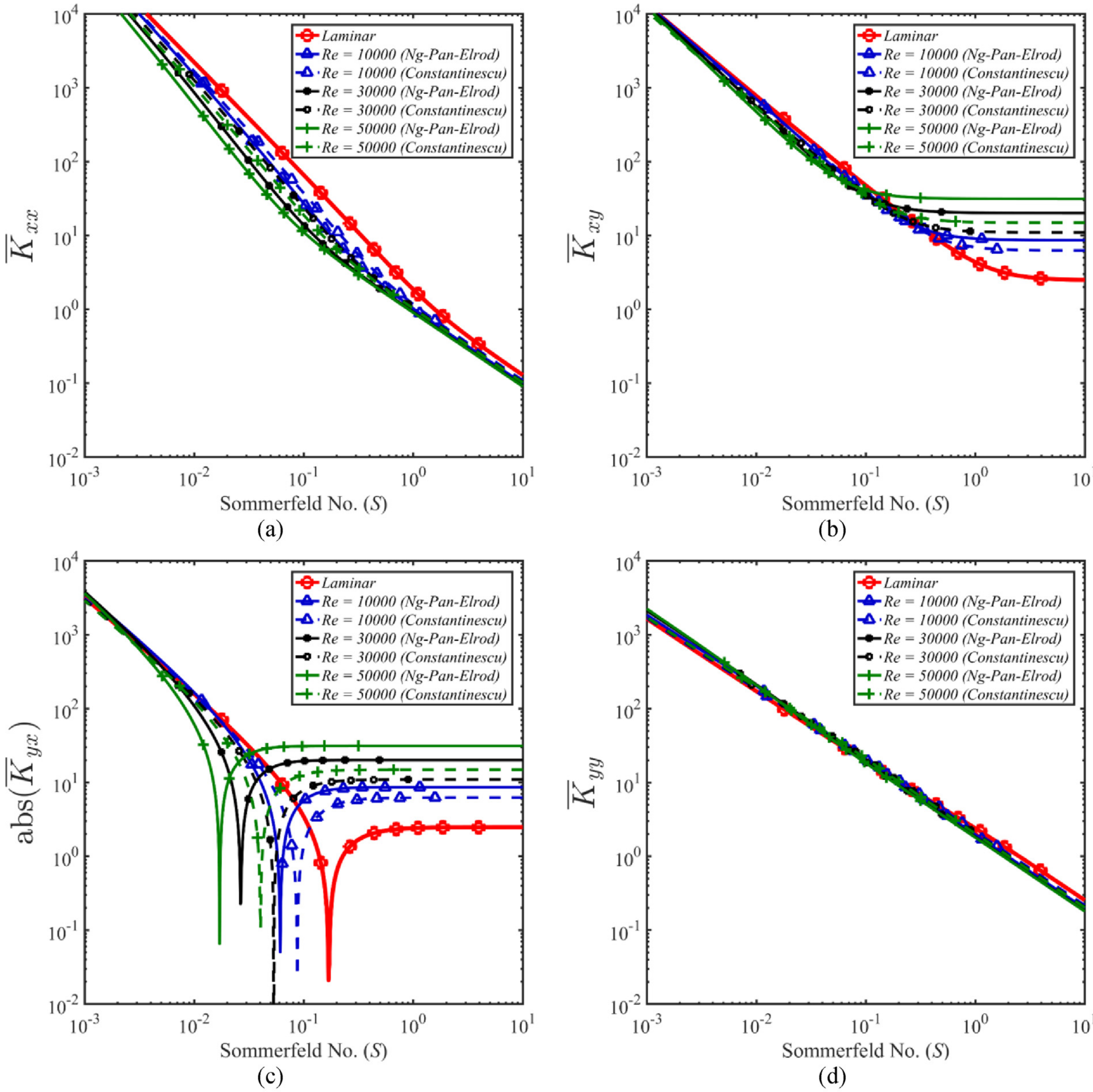

Fig. 4. Stiffness coefficients comparison of laminar and turbulent short journal bearings ($L/D = 0.5$), (a) $\bar{K}_{xx}$, (b) $\bar{K}_{xy}$, (c) $abs(\bar{K}_{yx})$, and (d) $\bar{K}_{yy}$.

however, this is not the case and will be discussed in more detail in Section 4. Similar treatment was carried out to calculate the damping coefficients of turbulent journal bearings. The calculated bearing damping coefficients in turbulent flow are compared to the calculated damping coefficients in the laminar region and are plotted against their corresponding Sommerfeld numbers which are plotted in Fig. 5. Although, direct damping coefficients increase by increasing the Reynolds number, cross-coupled coefficients remain steady. The results presented in Figs. 4, 5, and Table A1 do not fully agree with the results presented by Capone et al. [25], Wang and Khonsari [12], and Hashimoto et al. [11] possibly because previous methods relied on inaccurate turbulent force calculations.

3.2. Turbulent long bearing theory formulation

By long bearing approximation $(L/D) \geq 2$, it can be assumed longitudinal pressure distribution is constant $((\partial P/\partial \theta) \gg (\partial P/\partial z))$; thus, $\frac{\partial P}{\partial z} = 0$ and updated turbulence Reynolds' equation for long bearing theory can be written as:

$$\frac{\partial}{\partial \theta}\left(\frac{h^3}{k_\theta}\frac{\partial P}{\partial \theta}\right) = \frac{\mu C R^2}{2}((2\dot{\varphi} - \omega)\epsilon \mathrm{Sin}(\theta) + 2\dot{\epsilon}\mathrm{Cos}(\theta)) \tag{17}$$

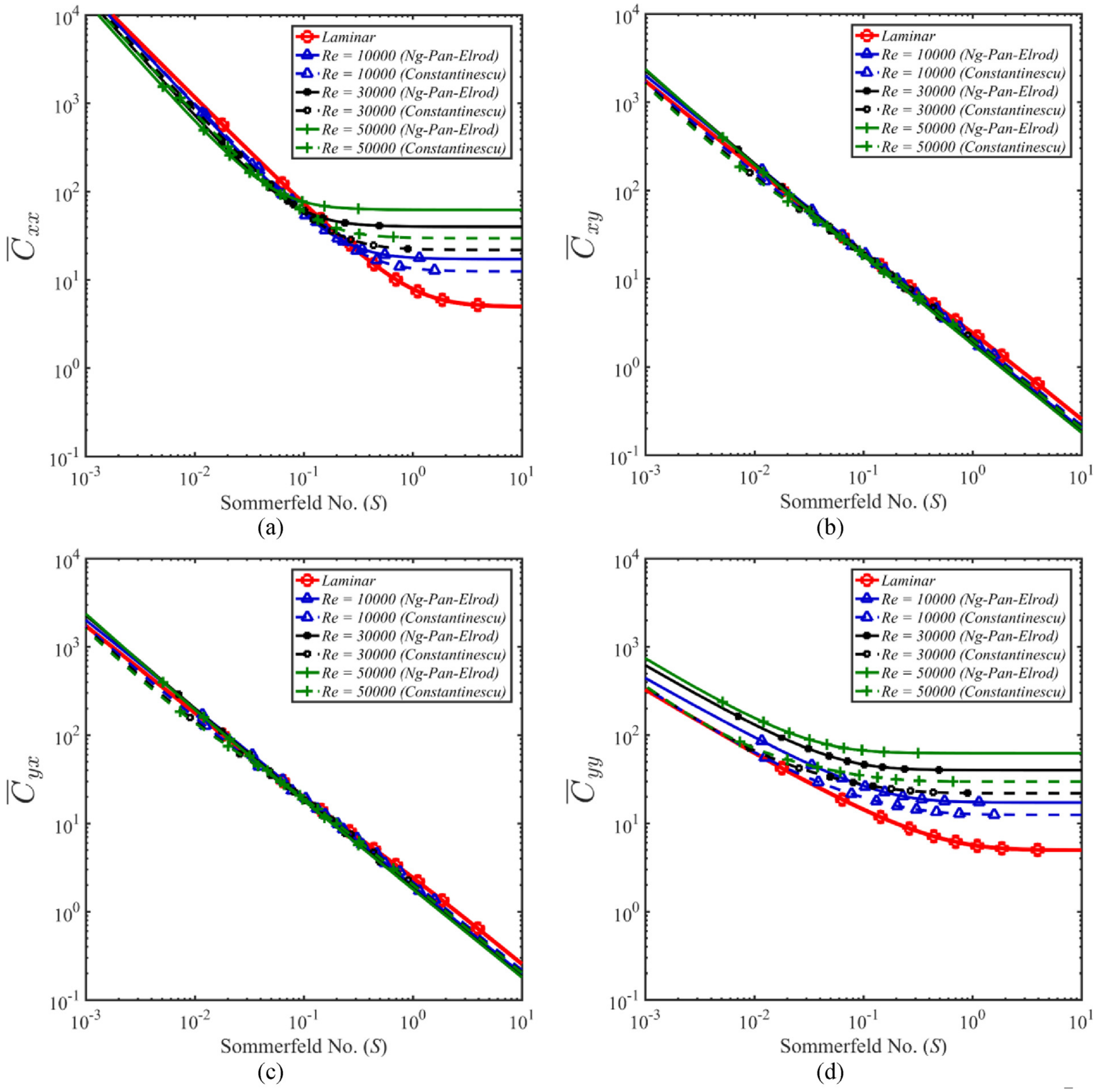

Fig. 5. Damping coefficients comparison of laminar and turbulent short journal bearings (L/D=0.5), (a) $\bar{C}_{xx}$, (b) $\bar{C}_{xy}$, (c) $\bar{C}_{yx}$, and (d) $\bar{C}_{yy}$.

The above equation can be integrated over θ to obtain the following equation:

$$\frac{\partial P}{\partial \theta} = \frac{k_\theta}{h^3}\left(\frac{\mu C R^2}{2}((\omega - 2\dot{\varphi})\epsilon \mathrm{Cos}(\theta) + 2\dot{\epsilon}\mathrm{Sin}(\theta)) + c_1\right)$$
$$= \frac{12 + \hat{a}_1\left(\overline{Re}\right)^{\hat{a}_2}((1+\epsilon \mathrm{Cos}(\theta)))^{\hat{a}_2}}{(C(1+\epsilon \mathrm{Cos}(\theta)))^3}\left(\frac{\mu C R^2}{2}((\omega - 2\dot{\varphi})\epsilon \mathrm{Cos}(\theta) + 2\dot{\epsilon}\mathrm{Sin}(\theta)) + c_1\right). \quad (18)$$

In order to be able to integrate the above equation to find an analytical expression for long bearing pressure, it is assumed $((1+\epsilon \mathrm{Cos}(\theta)))^{\hat{a}_2} \approx (1 + \hat{a}_3 \epsilon \mathrm{Cos}(\theta))$. The constant $\hat{a}_3$ may be found by curve fitting via optimization, which is calculated to be 0.8437, and 0.91 for Constantinescu and Ng–Pan–Elrod theories, respectively. By applying the aforementioned assumption along with applying Gümbel boundary condition, the non-dimensional form of the turbulent long bearing pressure can be written as:

$$\bar{P} = \frac{\pi\epsilon\left(\epsilon\sin(2\theta)\left(2\hat{a}_3^2H^2\epsilon^2 - (H+12)\left(\hat{a}_3H + H + 12\right)\right) + 2\sin(\theta)\left(\hat{a}_3H\epsilon^2\left(\hat{a}_3H + H + 12\right) - 2(H+12)^2\right)\right)}{2\left(\epsilon^2\left(\left(3\hat{a}_3 - 1\right)H - 12\right) - 2(H+12)\right)(\epsilon\cos(\theta) + 1)^2}, \tag{19}$$

where $H = \hat{a}_1(\overline{Re})^{\hat{a}_2}$. By substituting Eq. (19) into Eq. (9), analytical expression of polar turbulent forces for a long journal bearing can be derived as:

$$\begin{aligned}
F_r &= \frac{1}{16C^2\epsilon^2(\epsilon^2-1)^2(\pi\epsilon^2((3\hat{a}_3-1)H-12) - 2\pi(H+12))} \\
&\times \begin{pmatrix} 8R^3\mu L(\sqrt{1-\epsilon^2}\dot{\epsilon}(\hat{a}_3^2H^2\epsilon^2(\pi^2(6(1-\epsilon^2)^{3/2} + 9\epsilon^2 - 6) - 16\epsilon^4) - 2\hat{a}_3H(H+12)(\pi^2((1-\epsilon^2)^{3/2}(\epsilon^2+2) \\ + 3\epsilon^4 + 2\epsilon^2 - 2) - 16\epsilon^4) + (H+12)^2(\pi^2(\epsilon^2+2) - 16)\epsilon^2) + 2\pi\epsilon(\epsilon^2-1)(\hat{a}_3^2H^2(2\epsilon^2-3)\epsilon^3 \\ - \hat{a}_3H(\epsilon^2-1)\tanh^{-1}(\epsilon)(\epsilon^2((3\hat{a}_3-1)H-12) - 2(H+12)) + 2\hat{a}_3H(H+12)\epsilon - (H+12)^2\epsilon^3)(\omega - 2\dot{\varphi})) \end{pmatrix} \\
F_t &= \frac{8R^3\mu L}{64C^2(1-\epsilon^2)^{3/2}(\epsilon^4(3\hat{a}_3H - H - 12) - 2(H+12)\epsilon^2)} \\
&\times \begin{pmatrix} 4\pi\epsilon(\epsilon^2-1)(\hat{a}_3^2H^2\epsilon^2(-3\sqrt{1-\epsilon^2} - 2\epsilon^2 + 3) - \hat{a}_3H(H+12)(2 - \sqrt{1-\epsilon^2}(\epsilon^2+2)) + (H+12)^2\epsilon^2)(\omega - 2\dot{\varphi}) \\ + 16\sqrt{1-\epsilon^2}\dot{\epsilon}(\hat{a}_3^2H^2(2\epsilon^2-3)\epsilon^3 - \hat{a}_3H(\epsilon^2-1)\tanh^{-1}(\epsilon)(\epsilon^2((3\hat{a}_3-1)H-12) \\ - 2(H+12)) + 2\hat{a}_3H(H+12)\epsilon - (H+12)^2\epsilon^3) \end{pmatrix}.
\end{aligned} \tag{20}$$

The same approach may be applied to derive the analytical stiffness and damping coefficients (non-dimensional form) for a turbulent long journal bearing which are tabulated in Table A2. According to Table A2, turbulent coefficients for a long journal bearing are not functions of length to diameter ratio (L/D). The variation of non-dimensional stiffness and damping coefficients with respect to their corresponding Sommerfeld numbers in Cartesian coordinate system are plotted in Fig. 6 and Fig. 7, respectively. According to Figs. 6 and 7, turbulence has a huge effect on long journal bearings compare to short journal bearings.

It should be noted that, the discrepancy between the coefficients calculated based on Constantinescu and Ng–Pan–Elrod models is very small due to small difference between their circumferential turbulence coefficients (k_θ), shown in Fig. 2.

4. Equations of motions and linear stability analysis of short and long turbulent journal bearings

In an ideal and fully balanced rotor-bearing system, the shaft spins at its designed operating speed while the induced pressures inside end journals can support the weight of the shaft and hence there exists and equilibrium point where the journal center finds and stays there during the operation. This point is referred to as the static equilibrium position. If the rotor bearing system is undisturbed, the rotor will remain in its equilibrium position. For small disturbances, for instance small unbalance force, the shaft will no longer stays at the static equilibrium point and orbits via a closed elliptic curve around its equilibrium point. These are the harmonic solutions to a stable dynamic system operating in its stable region. If the operating speed of the shaft exceeds the so called threshold speed of instability ω_s, no stable harmonic solution exists and the journal orbit will spiral outward towards an either bounded stable limit cycle (with orbits generally much greater than the stable closed harmonic orbits) or towards the point where metal to metal contact occurs. This change of the dynamical behavior of the system is called a bifurcation and is known in rotor dynamics terminology as the oil whirl–whip phenomenon. It should be noted that oil whirl and rotor whirling will happen for both fully balanced and unbalanced rotor with the exception that the threshold speed of a balanced system is higher than the threshold speed of an unbalanced system. The transition (bifurcation) to high amplitude vibration, whether to a stable limit cycle or towards the bearing clearance, can be either gradual (supercritical bifurcation) or sudden (subcritical bifurcation). Bifurcation towards the limit cycle is generally considered as an unstable operating condition while it is not necessarily unstable. The reason for this is that the majority of the stability analysis available in the literature are based on linear analysis and from the viewpoint of linear analysis there is no difference between unstable and stable limit cycles (they are both considered as unstable). Even though the bifurcation type cannot be evaluated via linear analysis, the stability margin can indeed be identified by simple linear analysis. This is because that local stability of nonlinear and linearized systems is essentially the same. Linearized analysis will be used here to identify the stability margins of the system. To do this, one needs to find the threshold speed of instability for a given rotor-bearing system at any applied static load to the shaft. If the operating speed of the rotor is kept below this threshold speed, the system remains in its stable region and hence the operation is considered as safe. The analysis here is following from [9,26] with minor corrections. Fig. 8 illustrates a centrally loaded rotor-bearing system along with its coordinates used in this paper. In Fig. 8, O_j is the center of the journal bearing, O_M is the center of the central mass, and W is the load per bearing. The coordinates (x_1,y_1) and (x_2,y_2) are utilized to denote the dynamic positions of the journal bearings and central mass, respectively. Referring to Fig. 8, to analyze a flexible, center-loaded and perfectly balanced rotor symmetrically supported by two identical fluid-film journal bearings, the following assumptions are made:

- Deflection of the flexible shaft is small to allow the use of linear beam theory.

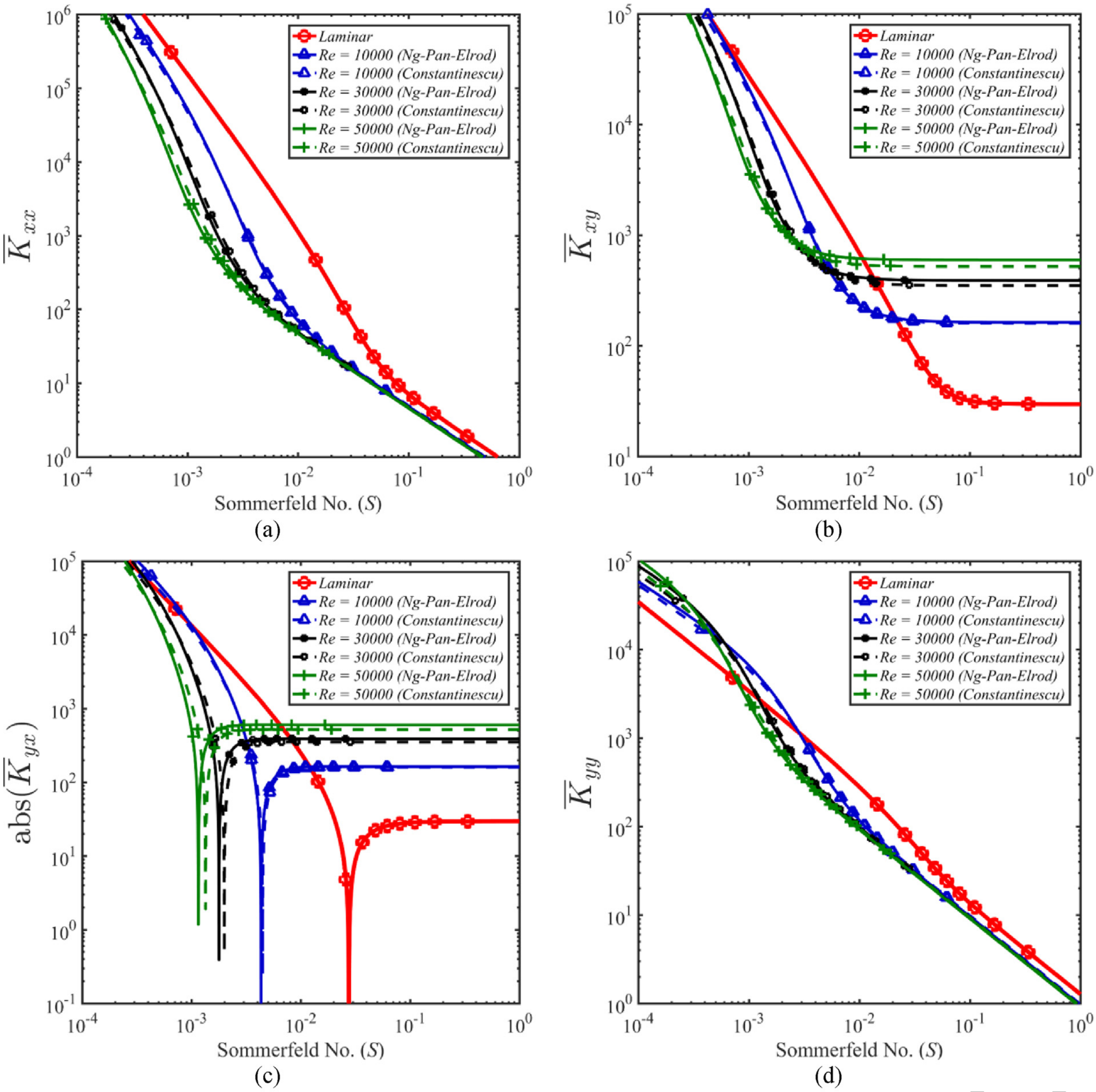

Fig. 6. Stiffness coefficients comparison of laminar and turbulent long journal bearings, (a) $\bar{K}_{xx}$, (b) $\overline{K}_{xy}$, (c) abs($\bar{K}_{yx}$), and (d) $\bar{K}_{yy}$.

- The mass of the shaft and rotor torque of the midpoint mass are negligible.
- The rotor mass is lumped at the midpoint.
- Axial and torsional vibrations of the lumped mass are negligible.
- Gyroscopic effect of the shaft, disk and journal bearings are negligible.

It should be noted that, K_s is the effective rotor stiffness which can be approximated as $192EI/L_S^3$. Where, L_s is the length of the shaft, E is shaft's Young's modulus, and I is its second moment of area. According to Newton's second law, the equations of motion for the central disk and journal bearings may be written as follows:

$$\text{Central Disk} \rightarrow \begin{cases} M\ddot{x}_2+K_s(x_2-x_1)=0 \\ M\ddot{y}_2+K_s(y_2-y_1)=0 \end{cases}$$
$$\text{Journal Bearings} \rightarrow \begin{cases} -2(K_{xx}x_1+K_{xy}y_1+C_{xx}\dot{x}_1+C_{xy}\dot{y}_1)+K_s(x_2-x_1)=0 \\ -2(K_{yx}x_1+K_{yy}y_1+C_{yx}\dot{x}_1+C_{yy}\dot{y}_1)+K_s(y_2-y_1)=0. \end{cases} \tag{21}$$

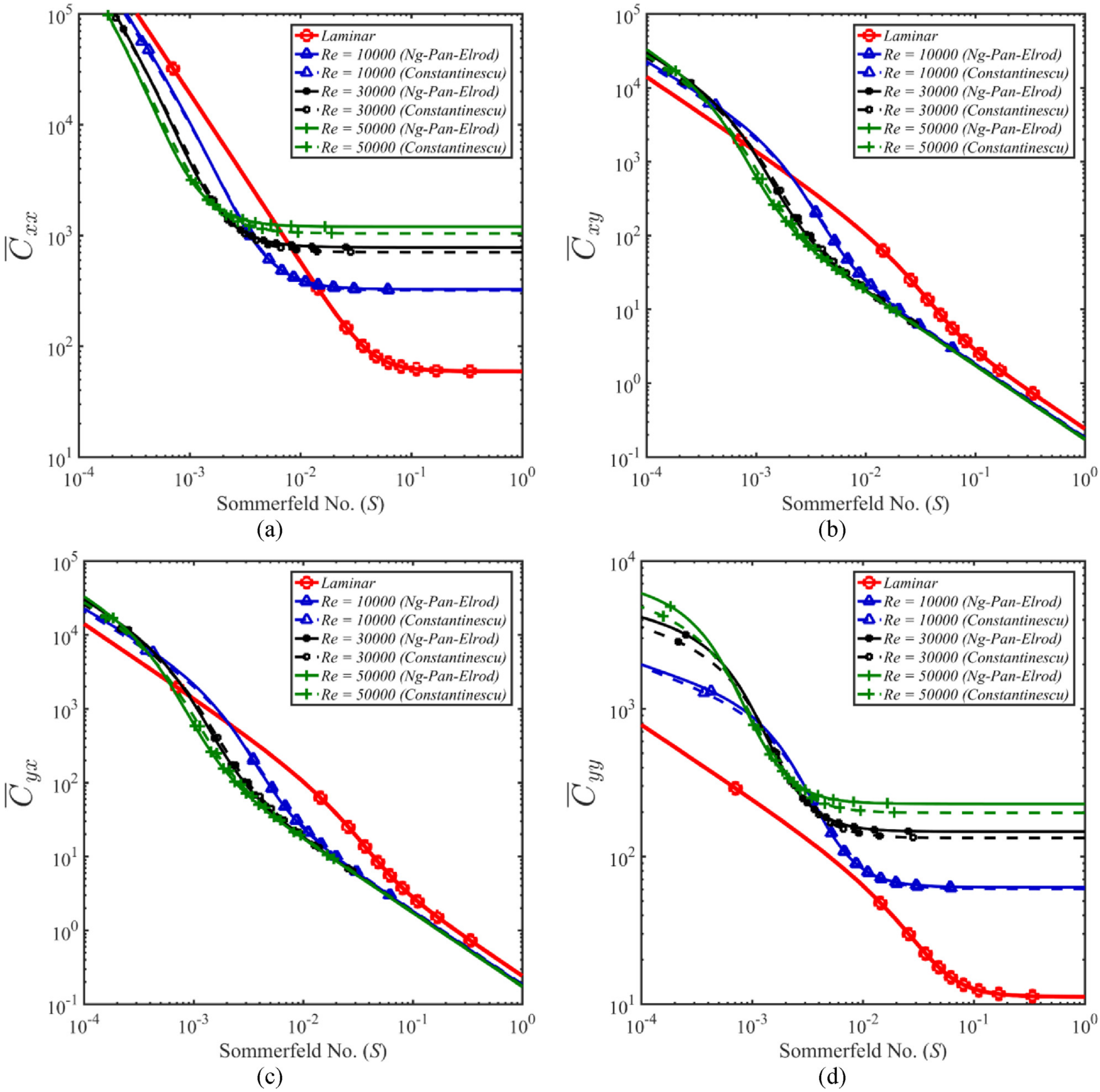

Fig. 7. Damping coefficients comparison of laminar and turbulent long journal bearings, (a) $\bar{C}_{xx}$, (b) $\bar{C}_{xy}$, (c) $\bar{C}_{yx}$, and (d) $\bar{C}_{yy}$.

If the system is running at the threshold speed of ω_s, then it can be assumed both journal bearings and central mass M will undergo whirl motion at frequency of ω_w; hence, their motions may be written as follows:

$$\begin{pmatrix} x_2 \\ y_2 \end{pmatrix} = \begin{pmatrix} X_2 \\ Y_2 \end{pmatrix} e^{i\omega_w t}, \quad \begin{pmatrix} x_1 \\ y_1 \end{pmatrix} = \begin{pmatrix} X_1 \\ Y_1 \end{pmatrix} e^{i\omega_w t}. \tag{22}$$

By making use of the derivations in Appendix A, the stability margins of short and long journal bearings for different non-dimensional stiffness coefficients of the shaft ($\frac{C\ K_s}{W}$) are calculated. Stability parameter $\bar{\Gamma} = \frac{C}{W} M\omega_s^2 = (\frac{C\ K_s}{W})\bar{\omega}_s^2 = S_z\bar{\omega}_s^2$ is plotted vs the Sommerfeld number as shown in Fig. 9 and Fig. 10 for short and long bearings, respectively, and the stable and unstable regions of operation are indicated.

From the stability plots of Figs. 9 and 10 it can be seen that as the non-dimensional shaft stiffness increases, the stable operating margin expands towards higher threshold speeds and hence the rotor-bearing system becomes stable at higher rotating spin speeds of the shaft. This trend remains valid through the whole loading range of both short and long bearings.

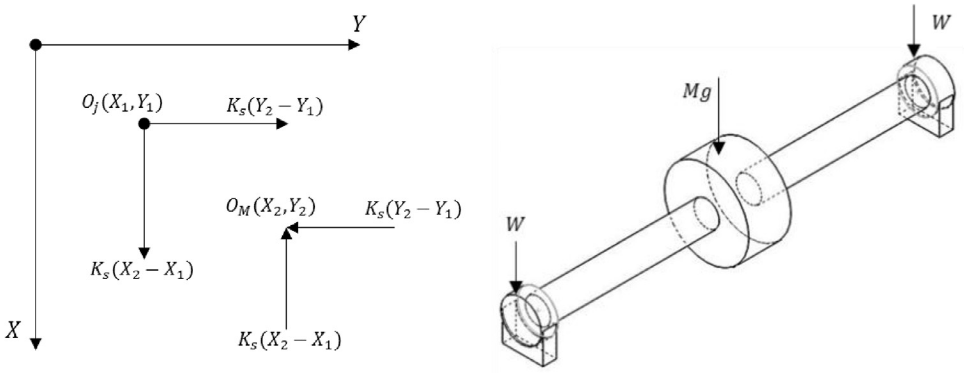

Fig. 8. Schematic of a flexible rotor supported on journal bearings. O_j and O_M correspond to the geometric center of the journal and the central disc, respectively.

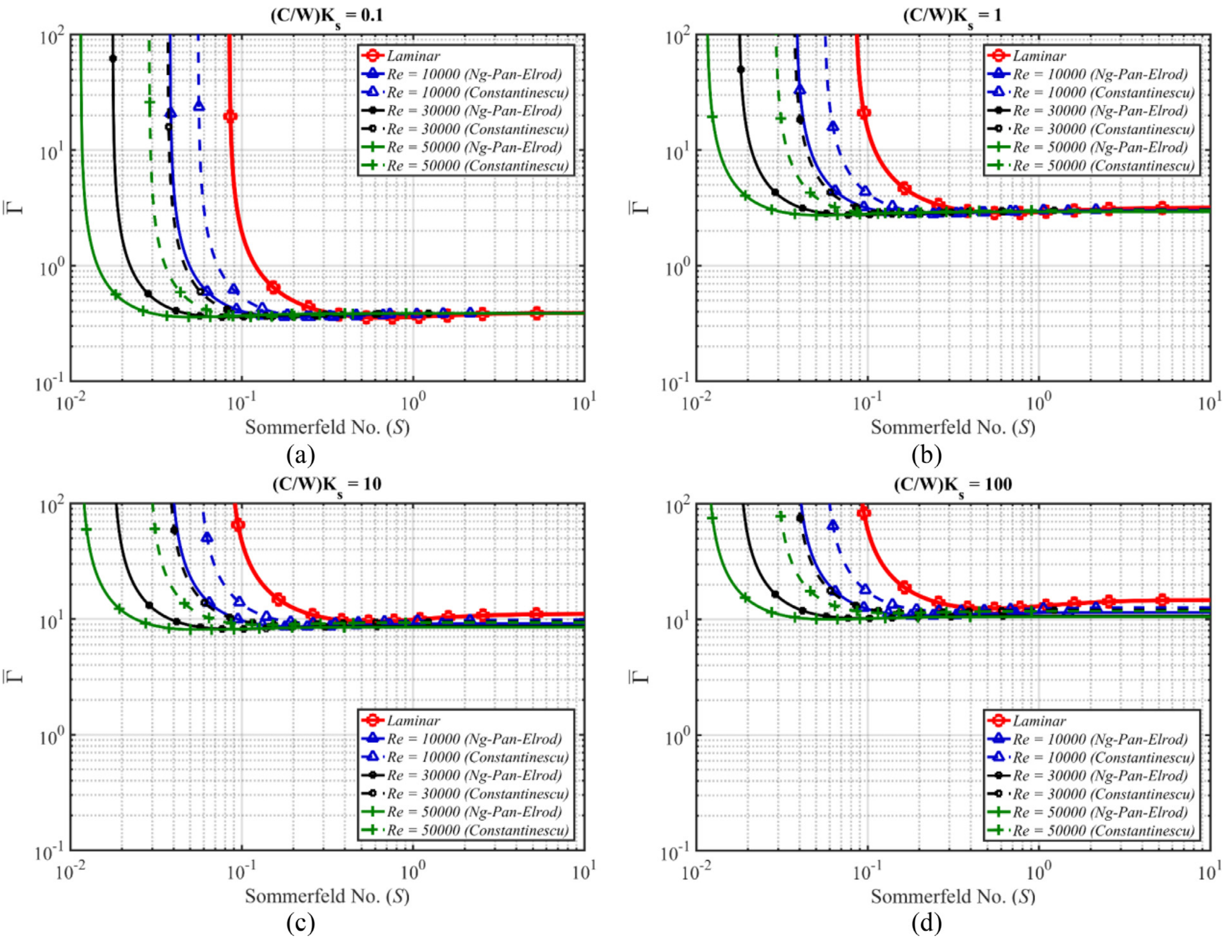

Fig. 9. Turbulent effects on the stability parameter $\bar{\Gamma}$ of a flexible shaft supported on short length journal bearings ($L/D=0.5$) at non-dimensional shaft stiffness coefficients of, (a) $\frac{C\,K_s}{W}=0.1$, (b) $\frac{C\,K_s}{W}=1$, (c) $\frac{C\,K_s}{W}=10$, and (d) $\frac{C\,K_s}{W}=100$.

By comparing Figs. 9 and 10, it may be concluded that, at a same shaft flexibility and Sommerfeld number, short bearings are more stable compare to long bearings. By comparing the stability of turbulent bearings to the laminar bearings and holding the non-dimensional shaft stiffness constant as in Figs. 9 and 10, it is clear that the turbulent curves are shifted to the left of the laminar curve, indicating that the unstable region has grown in size. As the static load increases (low Sommerfeld number), there is a limit of $S\cong 0.01$ and $S\cong 0.001$ for short and long bearings, respectively, in which further increase of the static load will not affect the stability of the system and system will remain stable at all operating speeds for

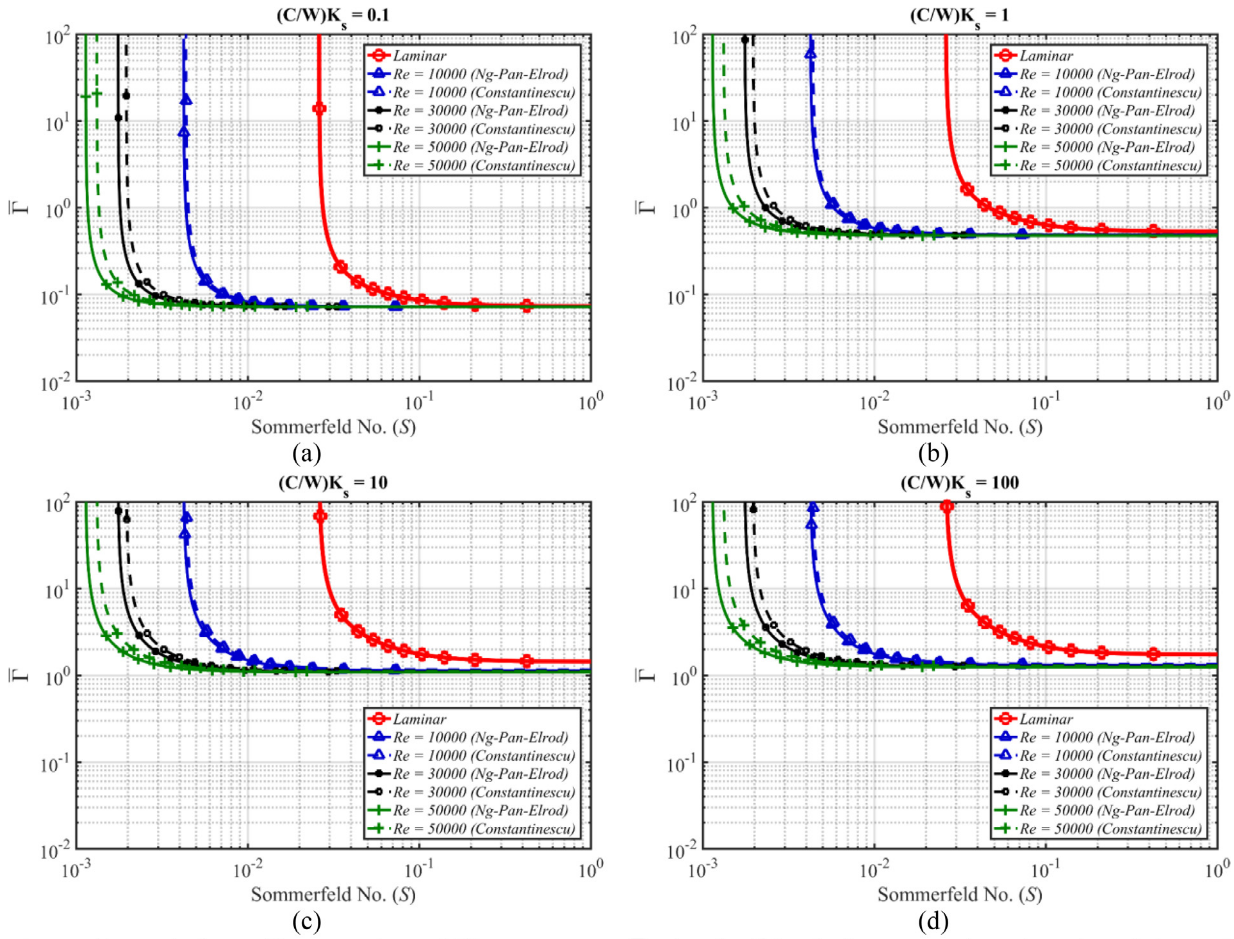

Fig. 10. Turbulent effects on the stability parameter $\bar{\Gamma}$ of a flexible shaft supported on long length journal bearings at non-dimensional shaft stiffness coefficients of, (a) $\frac{C\,K_s}{W} = 0.1$, (b) $\frac{C\,K_s}{W} = 1$, (c) $\frac{C\,K_s}{W} = 10$, and (d) $\frac{C\,K_s}{W} = 100$.

mean Reynolds numbers up to 50,000. This suggests that as the static loading increases on the shaft, the turbulent journal bearings are progressively less stable compared to the bearing which is operating in the laminar region of oil film flow. At high Sommerfeld region $S \geq 0.2$ (low load) the stability curves of laminar and turbulent bearings are very much alike for both short and long bearings. This destabilizing effect of turbulent bearings increases by the Reynolds number.

At each Reynolds and at each non-dimensional shaft stiffness, the stability curves of Constantinescu's turbulent model are positioned above the curves obtained based on the Ng–Pan–Elrod turbulent model suggesting that the Ng–Pan–Elrod turbulent treatment is more conservative when used as basis for design of the rotor-bearing system. To illustrate the expansion of the unstable operating region and shortcoming of the laminar theory to accurately predict the stable regions of the rotor-bearing system at high Reynolds numbers, the journal trajectories at different operating points should be calculated. To do this, the set of governing equations of motion for the journal and the shaft are to be numerically calculated to obtain the trajectory of the journal center. This is done first by writing the force balance at the journal center and mass center demonstrated in Fig. 8, along with weight of the shaft,

$$\begin{aligned}
&M\ddot{x}_2 + K_s(x_2 - x_1) - Mg = 0\\
&M\ddot{y}_2 + K_s(y_2 - y_1) = 0\\
&2(F_r\mathrm{Cos}(\varphi) - F_t\mathrm{Sin}(\varphi)) + K_s(x_2 - x_1) = 0\\
&2(F_r\mathrm{Sin}(\varphi) + F_t\mathrm{Cos}(\varphi)) + K_s(y_2 - y_1) = 0.
\end{aligned} \tag{23}$$

Normalizing Eq. (23), utilizing $\omega x_i' = \dot{x}_i$, $\omega y_i' = \dot{y}_i$, $\bar{x}_i = x_i/C$, $\bar{y}_i = y_i/C$, $\bar{F}_r = F_r(\frac{\pi C^2}{\mu\omega LR^3})$, and $\bar{F}_t = F_t(\frac{\pi C^2}{\mu\omega LR^3})$, the nonlinear dimensionless forms of the equations of motion may be written as:

$$\bar{x}_2'' + \frac{S_z}{\bar{\bar{\Gamma}}}(\bar{x}_2 - \bar{x}_1) - \frac{2}{\bar{\bar{\Gamma}}} = 0$$

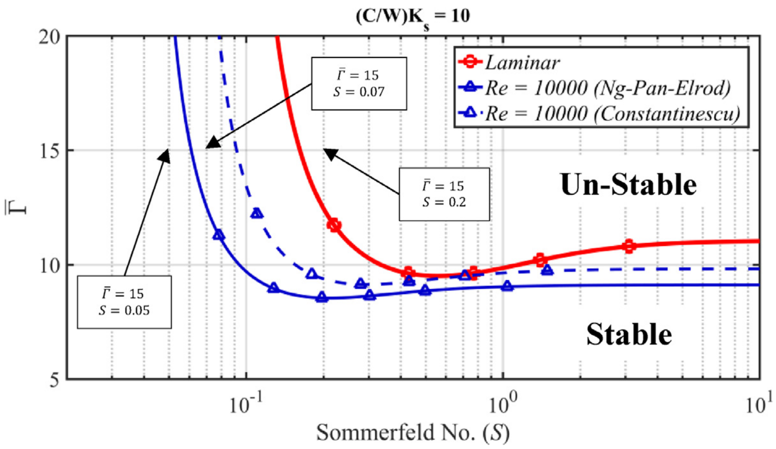

Fig. 11. Selected operating points under laminar and turbulent short journal bearings ($L/D{=}0.5$).

$$\bar{y}_2'' + \frac{S_z}{\bar{\Gamma}}(\bar{y}_2 - \bar{y}_1) = 0, \tag{24}$$

$$\begin{aligned} 2\bar{F}_r &= -\frac{S_z}{S}\left((\bar{x}_2 - \bar{x}_1)\frac{\bar{x}_1}{\sqrt{\bar{x}_1^2 + \bar{y}_1^2}} + (\bar{y}_2 - \bar{y}_1)\frac{\bar{y}_1}{\sqrt{\bar{x}_1^2 + \bar{y}_1^2}}\right) \\ 2\bar{F}_t &= \frac{S_z}{S}\left((\bar{x}_2 - \bar{x}_1)\frac{\bar{y}_1}{\sqrt{\bar{x}_1^2 + \bar{y}_1^2}} - (\bar{y}_2 - \bar{y}_1)\frac{\bar{x}_1}{\sqrt{\bar{x}_1^2 + \bar{y}_1^2}}\right), \end{aligned} \tag{25}$$

where $S_z = (\frac{C}{W})K_s$ is the non-dimensional form of shaft stiffness coefficient and S is the Sommerfeld number. It shall be noted that trajectories can be solely obtained based on the linearized coefficients provided that the journal position remains close to its steady state position. This in return can be very beneficiary since the computational cost of obtaining trajectories based on the linearized coefficients is much cheaper than obtaining the journal force and hence the trajectories at each time step by directly solving the Reynolds lubrication equation. System of Eq. (21) can be used as basis for calculation of the journal trajectories for much more complicated systems provided that the dynamic coefficients are available (either previously calculated or experimentally obtained). The system of coupled nonlinear ODEs of Eqs. (24) and (25) are integrated numerically by an explicit scheme in MATLAB to obtain the trajectories of the journal and the disk center. Non-dimensional journal trajectories, plot of $\bar{x}_1$ *vs* $\bar{y}_1$, at three different operating points were calculated based on both laminar and turbulent models (Constantinescu, Ng–Pan–Elrod models at $\overline{Re} = 10,000$). Trajectories of the selected operating points, shown in Fig. 11, are calculated for a short journal bearing ($L/D = 0.5,\ S_z = (\frac{C}{W})K_s = 10,\ \bar{\Gamma} = 15$) and demonstrated in Fig. 12. For all the cases shown in Fig. 12, the journal center trajectory is started at the position near by the center of the bearing, that are $\bar{x}_1 = 0.1/\sqrt{2}$, $\bar{y}_1 = 0.1/\sqrt{2}$, and trajectories are followed in time.

The first operating point is selected such that it lies in the unstable region of both laminar and turbulent curves at $S = 0.2,\ \bar{\Gamma} = 15$. Similar results were obtained where journal center grows fast in time from the turbulent models, Fig. 12(d) and (g). The next operating point $S = 0.07,\ \bar{\Gamma} = 15$ lies between the two different turbulent theories and on the stable region of the laminar curve. As expected, the laminar based trajectory along with Constantinescu hypothesis, Fig. 12(b), and (e) can still find their steady state point while the turbulent trajectory based on Ng–Pan–Elrod method, Fig. 12(h), start to grow and hence becomes unstable.

This again indicates that stable regions obtained based on the laminar theory can become unstable at higher Reynolds numbers. Both laminar and the two different turbulent trajectories find their static equilibrium points at $S = 0.05,\ \bar{\Gamma} = 15$ with different operating speeds, Fig. 12(c), (f), and (i). As it can be seen from Figs. 10, 11, and 12, Ng–Pan–Elrod turbulent model is more conservative than Constantinescu's model and has been utilized for nonlinear stability analysis at high Reynolds numbers where fluid regime is turbulent.

5. Application of Hopf bifurcation theory in flexible rotor bearing systems

Hopf bifurcation theorem characterizes local behavior of periodic solution (limit cycle) that bifurcates from a fixed point $\mathbf{x_e}$ when parameter μ is near a critical value μ_c. The Hopf bifurcation theory describes the birth of a periodic solution of a system whose behavior is defined by the ordinary differential equations $\dot{\mathbf{x}} = \mathbf{f}(\mathbf{x}, \mu),\ (\mathbf{x} \in R^n)$. A Hopf bifurcation occurs, when as the system parameter μ varies, a single complex conjugate pair of eigenvalues of the linearized system equations

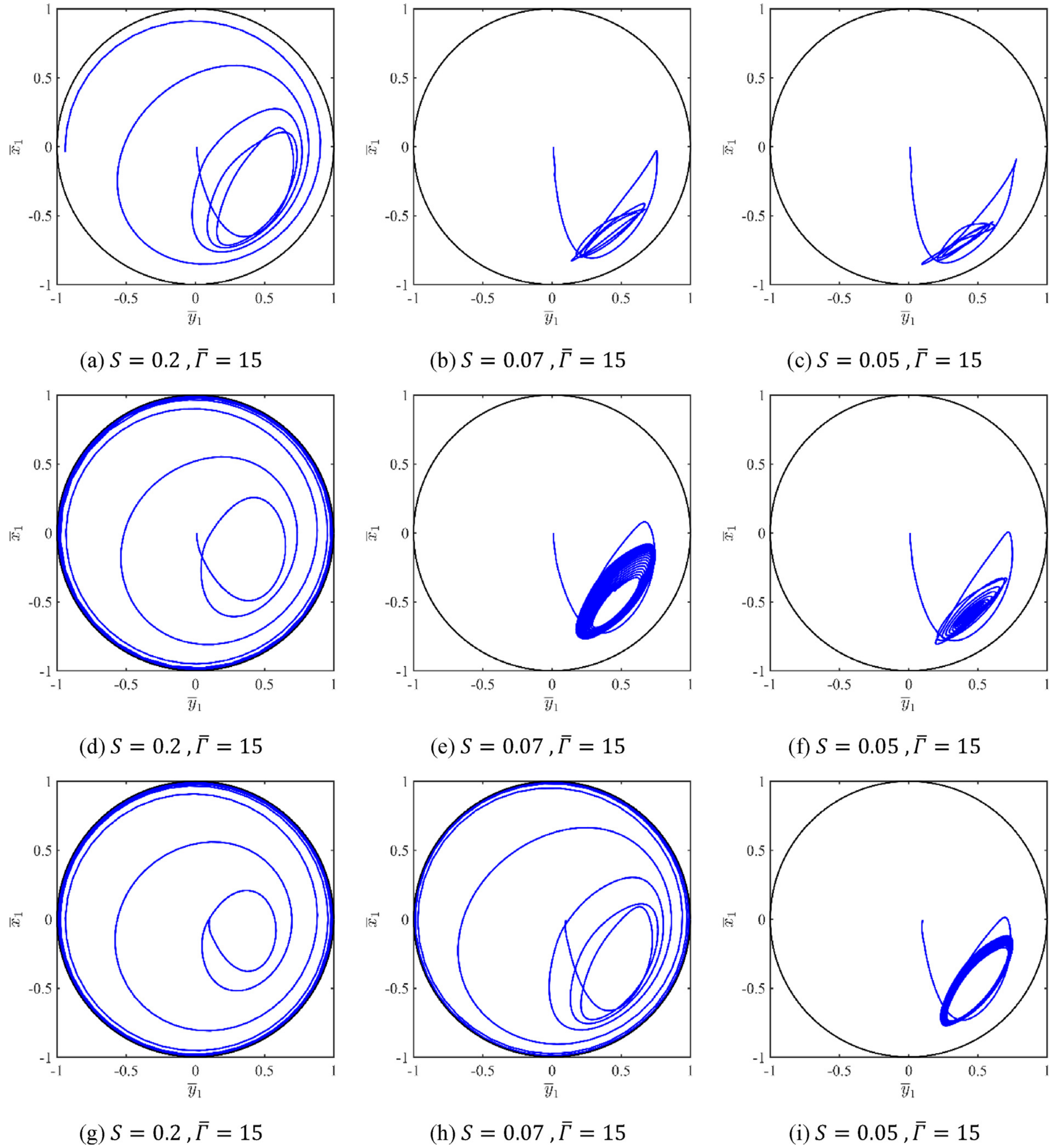

Fig. 12. Short journal bearing (L/D=0.5) trajectory at three operating points (a)–(c) under laminar flow, (d)–(f) under Constantinescu's turbulent model (g)–(i) under turbulent Ng–Pan–Elrod regime at Reynolds number of 10,000.

become purely imaginary (in the process of crossing the imaginary axis) [27]. The conditions that must be met for the Hopf bifurcation theory are [28]:

(i) Equation $\dot{\mathbf{x}} = \mathbf{f}(\mathbf{x}, \mu)$ must have an isolated stationary point at $\mathbf{x}=\mathbf{x_e}(\mu)$;

(ii) The Jacobian matrix $(\mathbf{A}(\mu) = (\frac{\partial f_i}{\partial x_j})(\mathbf{x_e}(\mu), \mu); i, j = 1, \ldots\ldots\ldots, n)$ has exactly a pair of complex conjugate eigenvalues $\lambda_{1,2}=\alpha(\mu) \pm i\beta(\mu)$ such that when $\mu=\mu_c, \alpha(\mu)=0$ and $\beta(\mu_c) > 0$. However, real part of the rest of the eigenvalues must be negative;

(iii) $\mathbf{f}$ is analytic in $\mathbf{x}$ and μ in the neighborhood of $(\mathbf{x}, \mu)=(\mathbf{x_e},\mu_c)$; and

(iv) $(d\alpha(\mu)/d\mu)(\mu_c) \neq 0$, where $\alpha(\mu)$ is the real part of the pair of eigenvalues that are continuous at μ_c.

In the above hypotheses, μ_c is called the critical value of μ. If assumption (ii) holds, then assumption (iv) implies that the linear stability of the stationary point $\mathbf{x_e}(\mu)$ will be lost as μ crosses μ_c. Under these conditions, at the onset of bifurcation, the system has a family of periodic solutions. The Hopf bifurcation theorem provides appropriate criteria for the prediction of the existence, shape, and period of the periodic solution [28]. In general (excluding the special case where bifurcation occurs only for $\mu \equiv \mu_c$), periodic solutions exist in exactly one of the cases: either $\mu > \mu_c$ or $\mu < \mu_c$ [29]. The periodic solutions in the case of $\mu > \mu_c$, is called a supercritical bifurcation. If the periodic solutions exist only in the case of $\mu < \mu_c$, then the system is said to undergo a so called subcritical bifurcation. The transition from steady state to limit cycle could be gradual (supercritical bifurcation) or sudden (subcritical bifurcation) and hence it is of absolute importance to identify the bifurcation type of a dynamical system. The equations of motion as given in Eqs. (24) and (25) have the suitable form of $\dot{\mathbf{x}} = \mathbf{f}(\mathbf{x}, \bar{\Gamma})$ and possess a steady state equilibrium position $\mathbf{x_s}$ for the application of the Hopf bifurcation theory. Here, the non-dimensional running speed $\bar{\Gamma}$ is considered as the system parameter when all other parameters of the rotor-bearing system are fixed. According to HBT, if the parameter $\bar{\Gamma}$ in the equations of motion (24) and (25) becomes greater than some critical value $\bar{\Gamma}_{cr}$, an isolated stationary point $\mathbf{x_s}(\bar{\Gamma})$ will lose its linear stability by having a complex conjugate pair of eigenvalues of the linearized system crossing the imaginary axis of the complex plane [27]. Hence, this critical value $\bar{\Gamma}_{cr}$ is the non-dimensional form of the threshold speed of instability of a rotor-bearing system. To implement the Hopf bifurcation analysis, first, the right hand side of the nonlinear equations of motion (24) and (25) is expanded in a Taylor series about the static equilibrium position ($\mathbf{x}=\mathbf{x_s}$) as follows;

$$\mathbf{f}\left(\mathbf{x}, \bar{\Gamma}\right) = \mathbf{f}\left(\mathbf{x_s}, \bar{\Gamma}\right) + \frac{\partial \mathbf{f}}{\partial \mathbf{x}}\left(\mathbf{x_s}, \bar{\Gamma}\right)\Delta\mathbf{x} + \frac{\partial^2 \mathbf{f}}{\partial \mathbf{x}^2}\left(\mathbf{x_s}, \bar{\Gamma}\right)\Delta\mathbf{x}^2 + \frac{\partial^3 \mathbf{f}}{\partial \mathbf{x}^3}\left(\mathbf{x_s}, \bar{\Gamma}\right)\Delta\mathbf{x}^3 + \mathrm{HOT}, \tag{26}$$

where $\Delta\mathbf{x}(\bar{\Gamma}) = \mathbf{x}(\bar{\Gamma}) - \mathbf{x_s}(\bar{\Gamma})$ and HOT represents the higher order terms in the Taylor expansion series. The zeroth order terms $\mathbf{f}(\mathbf{x_s}, \bar{\Gamma})$ are used to determine the static equilibrium position. The first order terms $\frac{\partial \mathbf{f}}{\partial \mathbf{x}}(\mathbf{x_s}, \bar{\Gamma})$, usually referred to as the Jacobian matrix of the equations of motion (24) and (25), are used to determine the dynamic performance through the analysis of the eigenvalues. The second order terms $\frac{\partial^2 \mathbf{f}}{\partial \mathbf{x}^2}(\mathbf{x_s}, \bar{\Gamma})$ and third order terms $\frac{\partial^3 \mathbf{f}}{\partial \mathbf{x}^3}(\mathbf{x_s}, \bar{\Gamma})$ are used to determine the stability of the periodic solutions. Specifically, the stability, the amplitude and the frequency of the periodic solutions are provided by these terms [27]. In this section, the Hopf bifurcation theory is used to predict the instability threshold speed and its bifurcation type at a range of operating conditions i.e. a range of Sommerfeld numbers (S). Bifurcation type (supercritical or subcritical) and stability boundary of a flexible rotor bearing system supported by short and long journal bearings are identified at different Reynolds numbers. Following the algorithm developed by Hassard et al. [28], a Hopf bifurcation subroutine was implemented using MATLAB to calculate the bifurcation parameters (μ_2 *and* β_2 [28] which are the Floquet exponents of the periodic solutions that determined their orbital stability) of the system. If $\beta_2 > 0$; periodic solutions exist for $\mu > \mu_{cr}$; and if $\beta_2 < 0$; periodic solutions exist for $\mu < \mu_{cr}$. Moreover, stability of the limit cycles can be determined from the stability parameter μ_2. If $\mu_2 < 0$; the solutions are orbital-asymptotically stable; however, if $\mu_2 > 0$; the solutions are orbital-asymptotically unstable. The bifurcation maps for flexible rotor-bearing systems are presented in Figs. 13 and 14 for short and long bearings at different Reynolds numbers. It should be noted that Ng–Pan–Elrod model was used to derive bifurcation maps in turbulent zones ($\overline{Re} \geq 2000$). Figs. 13 and 14 show that how the dimensionless instability threshold speed and its bifurcation type change with increasing the Sommerfeld number (S) for given dimensionless values of rotor stiffness (S_z). As it can be inferred from these figures, neglecting the rotor stiffness and turbulence effects may lead to erroneous results in the prediction of the instability threshold speed and its bifurcation type as the expansion of the unstable region with decreased shaft stiffness is neglected in stability curves that are obtained based on the rigid rotor assumption. Any solitary curve in Figs. 13 and 14 provides two pieces of information; (1) whether the system at any operating condition is stable or not for a range of Reynolds numbers; and (2) the bifurcation type at any point along the curve. The boundary line separating the stable and unstable regions is drawn in either solid or dashed lines according to the bifurcation type. If the bifurcation type is supercritical, a boundary line is drawn with a solid line whereas if the bifurcation type is subcritical, it is shown as a dashed line. Based on the linear theory of stability, when the operating speed exceeds the threshold speed of instability, the system is to be rendered unstable and any bifurcation is hence treated the same regardless of its type. However, the transition from stable to unstable could show significant difference depending on the bifurcation type. To better demonstrate this, two points corresponding to two different operating conditions are chosen along a stability curve. The first point is chosen to fall in the solid part of the curve (i.e. in the supercritical bifurcation region) and the latter in the region marked with dashed lines (i.e. in the subcritical bifurcation region). The journal trajectory at this operating condition is then found by integrating the equations of motion as the operating speed crosses the stability curve and are shown in Fig. 15(a) and (b). As it can be seen in Fig. 15, the amplitude of the journal lateral vibrations indeed grow after crossing the stable curve but this increase in amplitude of lateral vibrations is shown to be gradual as in Fig. 15(a) or sudden with ever increasing amplitudes as shown in Fig. 15(b).

As mentioned before, the Hopf bifurcation theory can be implemented in determining the bifurcation type as well as providing a local estimate of the limit cycle size (the amplitude of the periodic solutions). The limit cycle positioning (with respect to the critical point) and size can change depending on the bifurcation type and the magnitude of the bifurcations parameter (operating speed) compared to the critical bifurcation parameter (threshold speed of instability), respectively. Determining the shape and size of the limit cycle in the subcritical operating regions is of particular interest in designing a rotor bearing system. According to linear stability theory for a rotor-bearing system that is operating at speeds below

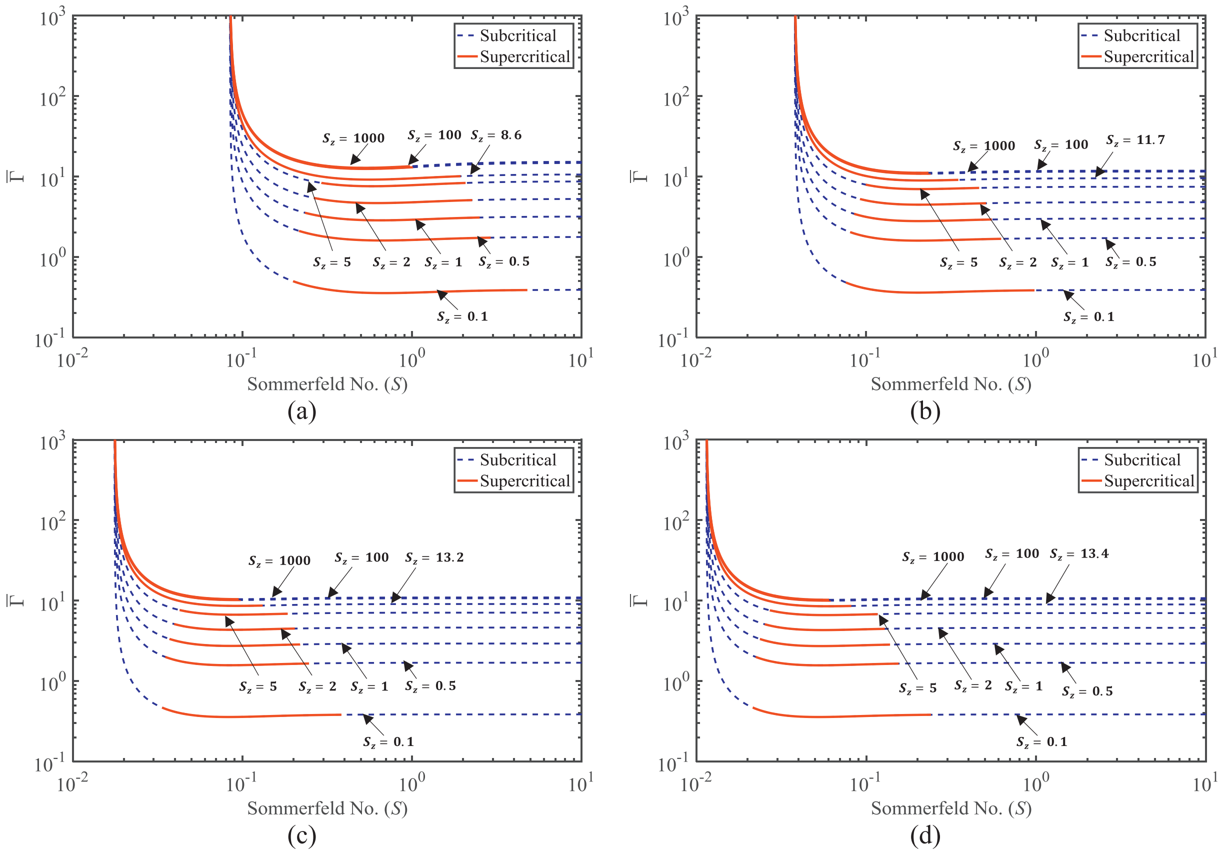

Fig. 13. Stability parameter $\bar{\Gamma}$ and its bifurcation type by increasing Sommerfeld number for a flexible shaft supporting on two identical short bearings (L/D=0.5), (a) laminar flow, (b) $\overline{Re} = 10,000$, (c) $\overline{Re} = 30,000$, (d) $\overline{Re} = 50,000$.

the threshold speed of instability, upon perturbing the system from its steady state operating point, the system finds its equilibrium state regardless of perturbation size (magnitude of the initial conditions).

Khonsari and Chang [30] reported that at certain operating conditions (being in the subcritical region), there exists a stability envelope that if the perturbation amplitude is greater than the amplitude of the envelope, the system can render unstable even at speeds below the threshold speed of instability. It was shown later [31] that the size of stability envelope can be precisely estimated by obtaining the size of the limit cycles as predicted in the hope bifurcation theorem [28]:

$$\mathbf{x}(t,\ \bar{\Gamma}) = \mathbf{x}_*(\bar{\Gamma}_c) + \sqrt{\frac{\bar{\Gamma} - \bar{\Gamma}_c}{\mu_2}}\mathbf{Re}\left(\mathbf{e}^{\frac{2\pi i t}{T}}\right) + \mathbf{o}(\bar{\Gamma} - \bar{\Gamma}_c)$$
$$T(\bar{\Gamma}) = \frac{2\pi}{\omega_0}\left(1 + \tau_2\left(\frac{\bar{\Gamma} - \bar{\Gamma}_c}{\mu_2}\right) + \mathbf{o}(\bar{\Gamma} - \bar{\Gamma}_c)^2\right), \tag{27}$$

where $T(\bar{\Gamma})$ is the period of the periodic solutions and τ_2 is the second exponent in the asymptotic expansion series of $T(\bar{\Gamma})$. Eq. (27) is used to calculate the boundary (shape) of the periodic solutions at a range of operating speeds near the threshold speed of instability for a rotor-bearing system operating in the subcritical region, the calculated boundaries are then plotted together to form a cone shape for both laminar and turbulent operating conditions as shown in Fig. 16(a) and (b). It shall be noted here that as the running speed crosses the threshold speed of instability, that is found by the means of linear analysis, a qualitative change happens in the dynamic response of the system which is called bifurcation. This bifurcation can have two subtypes: supercritical and/or subcritical. In the supercritical case, Stable periodic solutions are born after crossing the threshold value and gaining more spin speed. This periodic solution is referred to as a limit cycle. It is noteworthy to mention that in supercritical cases, periodic orbits do not exist at speeds below the threshold speed and even when they appear after crossing the threshold speed, their amplitude is small and tolerable. In the subcritical case; however, no stable periodic solution exists after crossing the threshold speed and system can become suddenly unstable. In such cases, unstable periodic orbits exist at speeds below the threshold speed. The cone shapes that are found in subcritical cases show the amplitudes of such periodic solutions. these regions can also reveal another interesting characteristic of the system: they show the allowable perturbation amplitudes that can be tolerated by the system i.e. if a shock is given to the

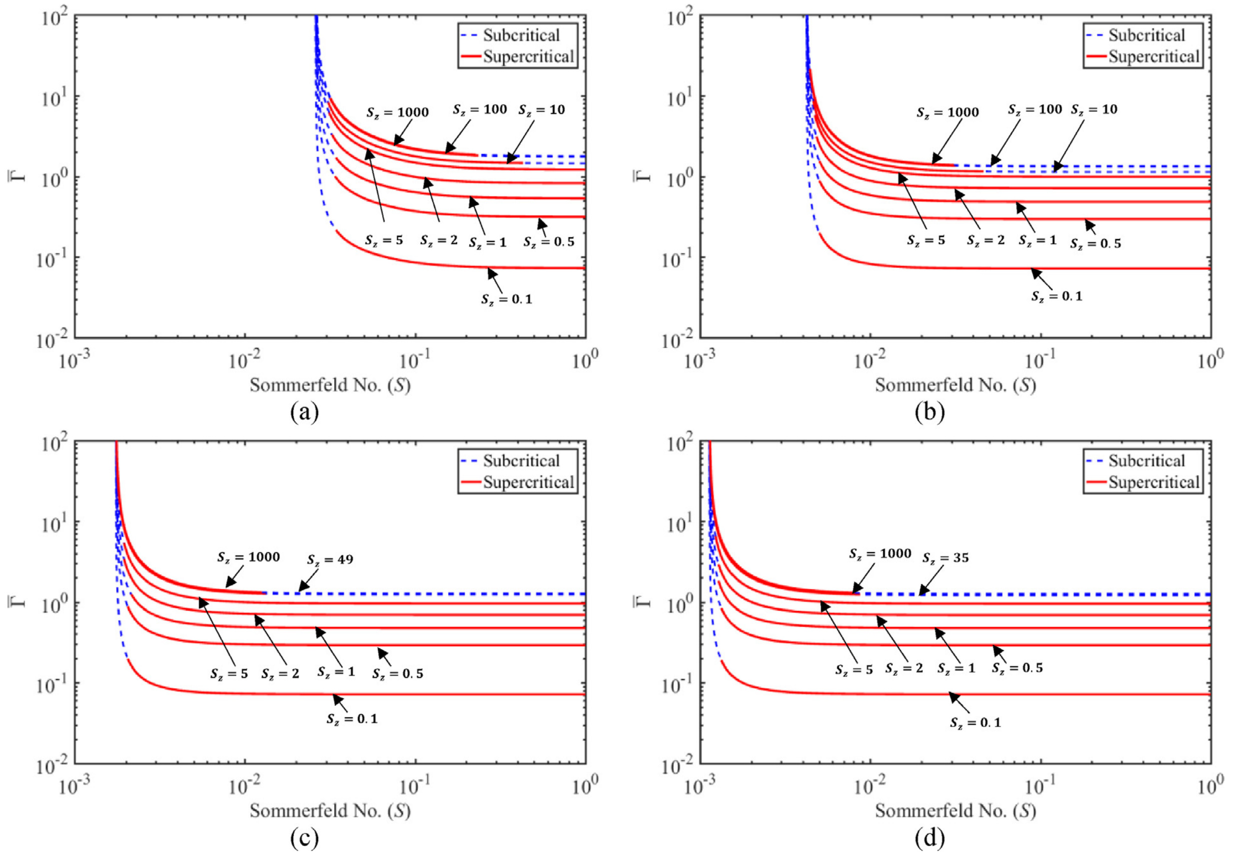

Fig. 14. Stability parameter $\bar{\Gamma}$ and its bifurcation type by increasing Sommerfeld number for a flexible shaft supporting on two identical long bearings, (a) laminar flow, (b) $\overline{Re} = 10,000$, (c) $\overline{Re} = 30,000$, (d) $\overline{Re} = 50,000$.

system with an amplitude confined within the cone, the system will find the steady state pure spinning mode. On the other hand, if the amplitude of the perturbation is big enough, outside the cone boundary, the system becomes unstable even though the operating running speed was below the threshold speed of instability. Such phenomenon cannot be explained by traditional linear stability analysis.

Since the bifurcation type for the selected operating point is subcritical, the unstable limit cycle exists at operating speeds less than the threshold speed of instability. The limit cycle amplitude decreases as the operating speed approaches the critical point and it ceases to exist after crossing the critical point. For a rotor-bearing system operating at speeds below the threshold speed, if the magnitude of an applied perturbation to the system is confined within the cone, the system will oscillate but the lateral vibrations amplitude will decrease and the system will find its steady state. However; if the perturbation magnitude is such that the journal is positioned outside the cone, the system will become unstable with ever increasing lateral vibration amplitudes even at speeds below the threshold speed of instability. Such phenomenon cannot be predicted by linear stability theory. To better compare the stability envelope in laminar vs turbulent operating conditions, a two-dimensional cut of the limit cycle cone is obtained from the cones in Fig. 16(a) and (b) and are re-plotted together in Fig. 17.

Fig. 16(a) and (b) show shapes of the periodic solutions of journal orbit as a function of dimensionless running speed that is close to but below the critical speed, $\bar{\Gamma}_c = 11.02$ and $\bar{\Gamma}_c = 9.11$ for laminar and turbulent regimes, respectively. Each cross section of Fig. 16(a) and (b) at a given dimensionless running speed $\bar{\Gamma}$ is the periodic solution of the journal orbit at this running speed. Fig. 16(a) and (b) show that the periodic solutions of journal orbit shrink to a single point as the running speed approaches the critical value $\bar{\Gamma}_c$. Fig. 17 shows the bifurcation profile, which depicts the amplitude of the periodic solution as a function of system running speed close to but below the critical speed $\bar{\Gamma}_c$. The subcritical bifurcation profile shrinks to a single point as the running speed approaches the critical value, $\bar{\Gamma}_c$. The amplitude of the periodic solution of the journal orbit corresponding to a specific running speed $\bar{\Gamma}$ is symmetrical at $\bar{\Gamma}_c$ and is bounded by $\epsilon_s \pm \sqrt{\frac{\bar{\Gamma}-\bar{\Gamma}_c}{\mu_2}}$. Where ε_s is the static equilibrium position of journal center at speed $\bar{\Gamma}_c$.

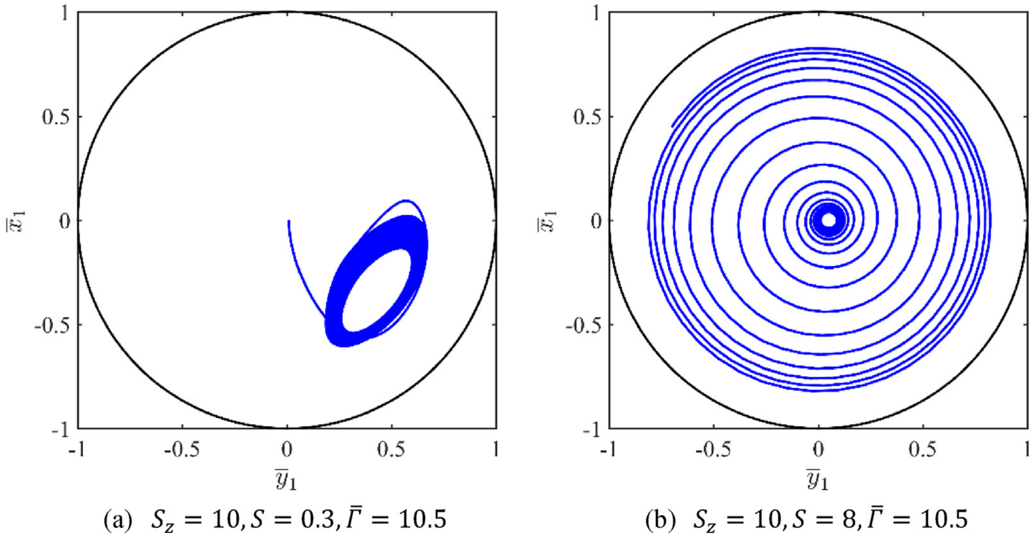

Fig. 15. Laminar short journal bearing ($L/D = 0.5$) trajectory at the speeds above the threshold speed of instability when operating at, (a) supercritical bifurcation region, (b) subcritical bifurcation region.

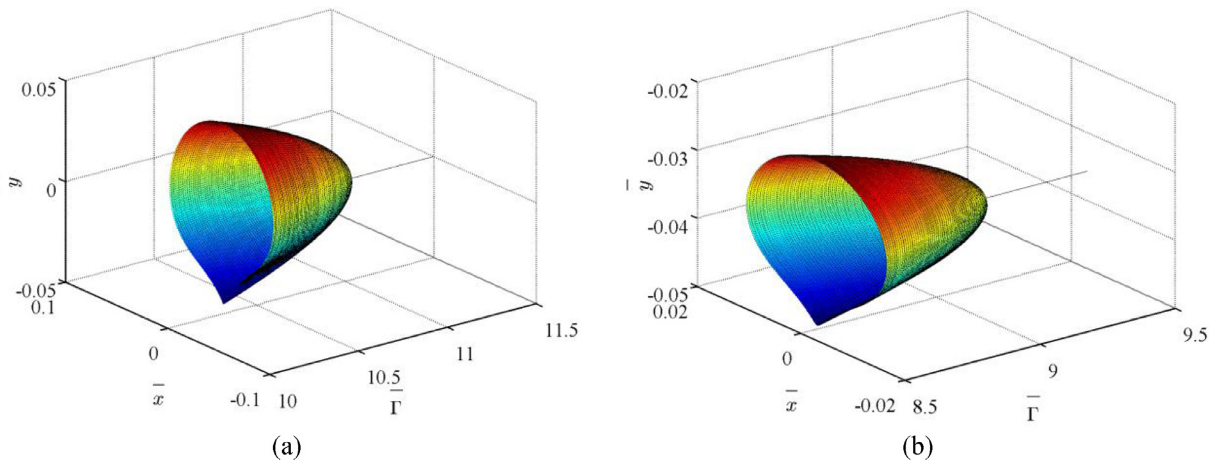

Fig. 16. Shapes of the periodic solutions of a short journal bearing ($L/D = 0.5$) at different running speeds. (a) Laminar model; (b) Ng–Pan–Elrod turbulent model ($\overline{Re} = 10,000$).

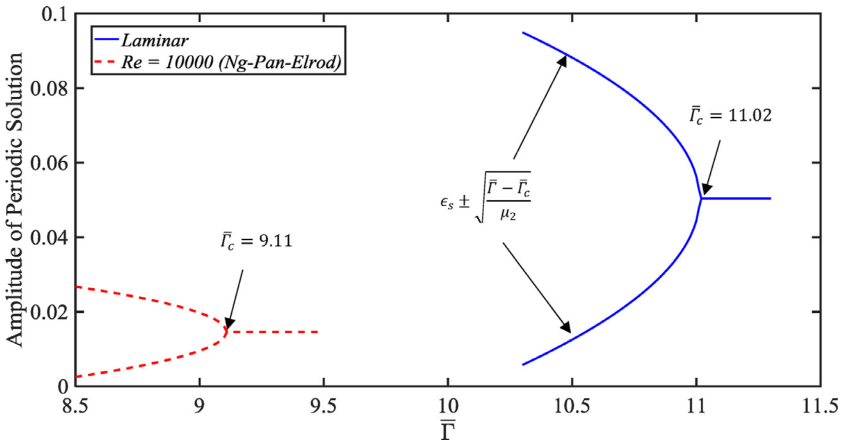

Fig. 17. Comparison of bifurcation profile of laminar vs. Ng–Pan–Elrod turbulent model ($\overline{Re} = 10,000$) of a short journal bearing ($L/D = 0.5$).

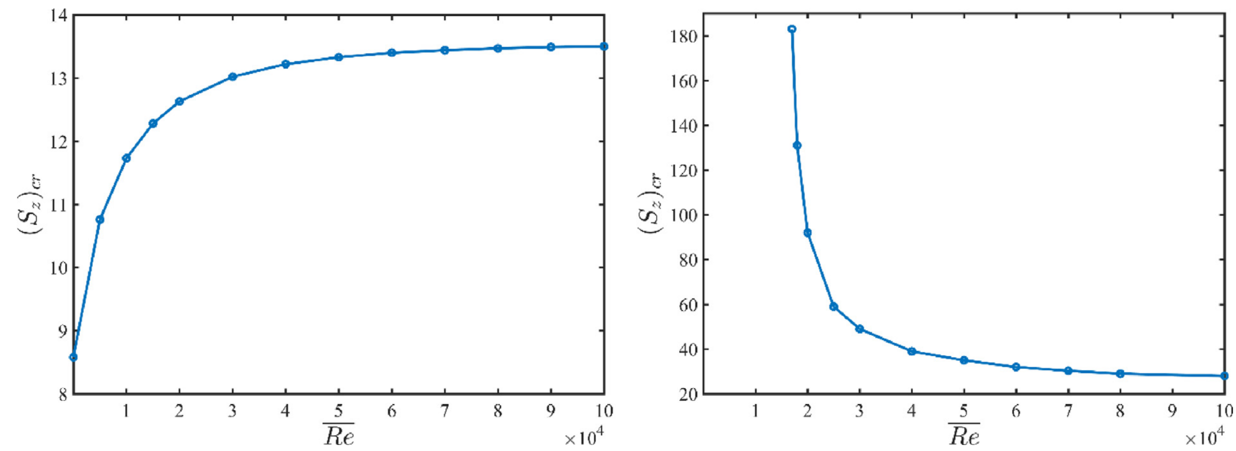

Fig. 18. Reynolds dependency of the critical stiffness of a flexible shaft supported on; (a) short journal bearings ($L/D = 0.5$), and (b) long journal bearings ($L/D \geq 2$).

Table 2
Specification of the rotor-bearing system for experimental verification [15].

Journal bearing diameter (D)	0.0254 m
Journal bearing length (L)	0.0127 m
Span length between two bearings	0.05271
Inside diameter of the hollow shaft	0.0152 m
Rotor mass (M)	5.4523 kg
Journal bearing clearance (C)	50.8×10^{-6} m
Lubricant type	ISO 32
Inlet pressure	31 kPa
Inlet temperature	20°C–100°C

From Fig. 17, it can be easily identified that as the oil flow region within the bearing chamber is transitioned from laminar into turbulent, the stability envelope shrinks in size whereas the whole stable boundary is shifted leftward, further expanding the unstable regions of operation.

Figs. 13 and 14 reveal that rotor stiffness has a pronounced influence on system's instability threshold speed and its bifurcation type. If the dimensionless rotor stiffness (S_z) is below its critical value, three bifurcation regions (by increasing Sommerfeld there are, subcritical, supercritical, and subcritical regions) exist, and if it is greater than its critical value, two bifurcation regions (by increasing Sommerfeld there are, supercritical and subcritical regions) exist. According to Figs. 13 and 14, the critical stiffness of the shaft is a strong function of the Reynolds number. The critical stiffness of a flexible shaft supported on short and long bearings are calculated at different Reynolds numbers using Ng–Pan–Elrod turbulent model and demonstrated in Fig. 18(a) and (b).

As it is shown in Fig. 18(a) and (b), the critical shaft stiffness strongly depends on Reynolds number at relatively low values for both short and long bearing supported shafts. For the case of short bearing supported shafts, the critical dimensionless shaft stiffness increases by increasing the Reynolds number and becomes steady after $\overline{Re} = 70,000$. However, for the case of long bearing supported shafts, the critical dimensionless shaft stiffness decreases by increasing the Reynolds number and becomes steady after $\overline{Re} = 70,000$. It should be noted that, critical dimensionless shaft stiffness does not exist at very low Reynolds numbers ($0 \leq \overline{Re} < 17,000$) for long bearing supported shafts. This suggest that for a shaft supported on long bearings operating at low Reynolds numbers, increasing shaft stiffness cannot suppress the subcritical region at low Sommerfeld numbers.

5.1. Experimental verification

Wang and Khonsari[15] designed and tested an experimental test rig for a flexible shaft supported on end journal bearings and identified the threshold speed of instability and bifurcation types for a range of bearing parameters. Bearing parameters are tabulated in Table 2. Their experimental results for a flexible shaft with non-dimensional half-shaft stiffness of$S_z = (\frac{C}{W})K_s = 1.45$ is plotted with the numerical predictions based on the mathematical model of this paper as shown in Fig. 19. The experimental results are for laminar short bearing assumption as $\overline{Re} \leq 200$.

As it can be seen from the Fig. 19, there is good agreement in threshold speed calculation as well as a qualitative agreement on bifurcation types between the numerical predictions and the experimental results. Both results suggest a transition from supercritical to subcritical bifurcation as bearing parameter increases. The difference from the analytical estimates and

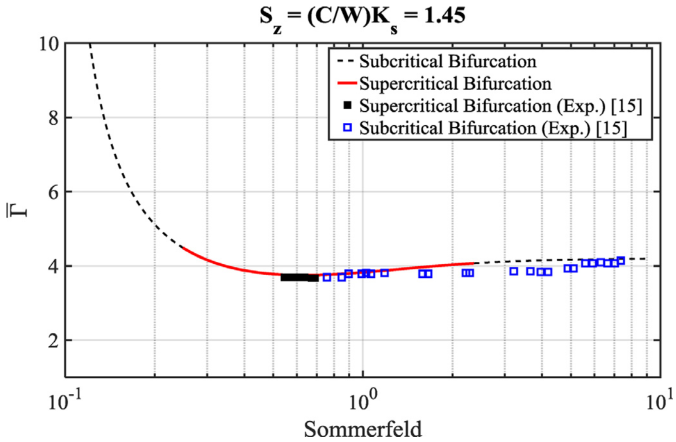

Fig. 19. Comparison between experimental and theoretical results with $S_z = 1.45$.

the experiments is due to simplifications in the mathematical model such as perfectly balanced rotor, neglecting the fluid inertia, short bearing assumption, neglecting temperature dependence of oil viscosity, and shaft gyroscopic effects, as well as the simplifying assumption of concentrated mass at the shaft center.

6. Conclusions and remarks

In the current study, the stability of flexible shaft supported on end journal bearings was studied for a range of operating conditions in both laminar and turbulent flow bearings and for different available turbulent models. The dynamic oil film forces considering the turbulent effects were obtained analytically under the short and long bearing assumption considering the Gümbel boundary condition. The closed form expressions for eight spring and damping coefficients were derived by linearizing the turbulent oil film forces around the steady-state equilibrium position of the journal center for two available turbulent models. The calculated dynamic coefficients were then utilized to obtain the whirl onset velocity for a flexible rotor supported by two identical journal bearings at various Reynolds numbers. Stable operating region of flexible shafts supported on both turbulent and laminar journal bearings were shown to grow in size by increasing the shaft non-dimensional stiffness parameter. It was found that at low load and high Sommerfeld regions $S \geq 0.2$ the stability would not be affected by the type of flow within the bearing chamber. On the other hand, as the static load on shaft increases in magnitude (i.e. lower Sommerfeld numbers), the unstable operating region grows in size and will result in the unstable oil whirl to happen at even higher static loads, a region where the laminar based stability analysis would consider as safe operating condition. Results also showed that predicted threshold speed of instability based on Constantinescu's model are higher than the threshold speeds predicted by the Ng–Pan–Elrod turbulent model and hence the latter model proves to be more conservative in design.

The Hopf bifurcation theory was used to study the orbital stability of periodic solutions near bifurcating points of the rotor bearing system, i.e. when the operating spin speed of the shaft is close to its threshold speed of instability. A Hopf bifurcation subroutine was written in MATLAB to calculate bifurcation parameters. The calculated bifurcation parameters were used to identify subcritical and supercritical regions along the path of whirl onset boundaries (curves separating stable and unstable operating regions). Subcritical regions were found to be more prevalent at high static loads (low Sommerfeld numbers). The width of dangerous subcritical regions was shown to be a function of the shaft stiffness. The stability envelope for subcritical operating regions were found for both laminar and turbulent operating conditions. The smaller the size of the stability envelope, the rotor bearing system is more susceptible to applied external perturbations. It was shown that the size of the stability envelope does indeed shrink as the flow region is transitioned from laminar to turbulent and hence it is crucial to study turbulent effects at high Reynolds numbers to precisely estimate the susceptibility of the rotor bearing system to externally applied perturbations. A critical shaft stiffness value was found at any Reynolds number, beyond which the unstable low Sommerfeld region can be transformed supercritical (hence stable) for a majority of operating conditions. The calculated critical shaft stiffness was found to be a strong function of the Reynolds number at relatively low Reynolds numbers for both short and long bearing supported shafts. However, the Reynolds dependence of the critical shaft stiffness parameter follows different trends for short and long bearings. While the critical stiffness constantly grows in size with increasing Reynolds number in short bearing supported shafts, the critical stiffness for long bearing supported shafts decreases with Reynolds number and it ceases to exist at low Reynolds numbers. This suggest that for a shaft supported on long bearings operating at low Reynolds numbers, increasing shaft stiffness cannot suppress the unstable critical region. It is hence recommended that for shafts under high static loads, better design choice would be a bearing with low length to diameter ratio to avoid the unstable subcritical regions of operation. As bearing performance is strongly dependent on lubricant viscosity and since viscosity of common lubricants strongly depends on the oil temperature, the results of classical theory can be expected to apply only in cases where the temperature raise in lubricant is negligible across the bearing pad. A proper cavitation model needs to be developed to accurately calculate short and long bearing pressure under laminar and turbulent conditions. To correctly predict the bearing performance required for precise identification of instability phenomenon, both the flow regime (being laminar or turbulent), variation of lubricant viscosity, as well as cavitation need to be taken into account and the stability curves found here should be modified to include this effect. This modification is the subject of future work to the current paper.

Experimental results in the literature are presented confirming the validity of the bifurcation diagram for flexible rotor-bearing system shown in Fig. 8 and its practicality for design purposes.

Acknowledgment

Author would like to thank Qatar National Research Fund (QNRF) for partially funding this project

Appendix A

Table A1
Analytical stiffness and damping coefficients for turbulent short bearings.

	Turbulent short bearing coefficients (Gümbel boundary condition)
$\bar{k}_{rr}$	$\frac{\pi}{6}(\frac{L}{D})^2\{\frac{48\epsilon(1+\epsilon^2)}{(1-\epsilon^2)^3}+(\frac{(1-\epsilon)^{a_2-2}-(1+\epsilon)^{a_2-2}}{(a_2-2)(a_2-1)\epsilon^2}+\frac{(1-\epsilon)^{a_2-3}((a_2-2)\epsilon+1)-(1+\epsilon)^{a_2-3}((a_2-2)\epsilon-1)}{(a_2-1)\epsilon})a_1(\overline{Re})^{a_2}\}$
$\bar{k}_{rt}$	$-(\frac{L}{D})^2(\frac{\pi}{\epsilon\sqrt{12}})^2\{\frac{-12\epsilon^2}{(1-\epsilon^2)^{3/2}}+(2a_4-\frac{\epsilon^2+a_4(2-3\epsilon^2)}{(1-\epsilon^2)^{3/2}})a_1(\overline{Re})^{a_2}\}$
$\bar{k}_{tr}$	$-(\frac{L}{D})^2(\frac{\pi^2}{12})\{\frac{12(1+2\epsilon^2)}{(1-\epsilon^2)^{5/2}}+(\frac{2a_4(1-\epsilon^2)^{5/2}+2\epsilon^4+\epsilon^2-a_4(6\epsilon^4-5\epsilon^2+2)}{(1-\epsilon^2)^{5/2}\epsilon^2})a_1(\overline{Re})^{a_2}\}$
$\bar{k}_{tt}$	$-(\frac{L}{D})^2(\frac{\pi}{6})\{\frac{-24\epsilon}{(1-\epsilon^2)^2}+(\frac{(1-\epsilon)^{a_2-2}+(1+\epsilon)^{a_2-2}}{(a_2-1)\epsilon}+\frac{(1-\epsilon)^{a_2-2}-(1+\epsilon)^{a_2-2}}{(a_2-2)(a_2-1)\epsilon^2})a_1(\overline{Re})^{a_2}\}$
$\bar{c}_{rr}$	$(\frac{L}{D})^2(\frac{\pi^2}{6})\{\frac{12(1+2\epsilon^2)}{(1-\epsilon^2)^{5/2}}+(\frac{2a_3(1-\epsilon^2)^{5/2}+2\epsilon^4+\epsilon^2-a_3(6\epsilon^4-5\epsilon^2+2)}{(1-\epsilon^2)^{5/2}\epsilon^2})a_1(\overline{Re})^{a_2}\}$
$\bar{c}_{rt}$	$-(\frac{L}{D})^2(\frac{\pi}{3})\{\frac{24\epsilon}{(1-\epsilon^2)^2}-(\frac{(1-\epsilon)^{a_2-2}+(1+\epsilon)^{a_2-2}}{(a_2-1)\epsilon}+\frac{(1-\epsilon)^{a_2-2}-(1+\epsilon)^{a_2-2}}{(a_2-2)(a_2-1)\epsilon^2})a_1(\overline{Re})^{a_2}\}$
$\bar{c}_{tr}$	$-(\frac{L}{D})^2(\frac{\pi}{3})\{\frac{24\epsilon}{(1-\epsilon^2)^2}-(\frac{(1-\epsilon)^{a_2-2}+(1+\epsilon)^{a_2-2}}{(a_2-1)\epsilon}+\frac{(1-\epsilon)^{a_2-2}-(1+\epsilon)^{a_2-2}}{(a_2-2)(a_2-1)\epsilon^2})a_1(\overline{Re})^{a_2}\}$
$\bar{c}_{tt}$	$-(\frac{L}{D})^2(\frac{\pi}{\epsilon\sqrt{6}})^2\{\frac{-12\epsilon^2}{(1-\epsilon^2)^{3/2}}+(2a_4-\frac{\epsilon^2+a_4(2-3\epsilon^2)}{(1-\epsilon^2)^{3/2}})a_1(\overline{Re})^{a_2}\}$
S	$\frac{12(\frac{D}{L})^2}{\pi\sqrt{(\frac{12\pi\epsilon}{(1-\epsilon^2)^{3/2}}-(2a_4-\frac{\epsilon^2+a_4(2-3\epsilon^2)}{(1-\epsilon^2)^{3/2}})(\frac{\pi}{\epsilon})a_1(\overline{Re})^{a_2})^2+4(\frac{24\epsilon^2}{(1-\epsilon^2)^2}+(\frac{(1-\epsilon)^{a_2-2}+(1+\epsilon)^{a_2-2}}{(a_2-1)\epsilon}+\frac{(1-\epsilon)^{a_2-2}-(1+\epsilon)^{a_2-2}}{(a_2-2)(a_2-1)\epsilon^2})a_1(\overline{Re})^{a_2})^2}}$
$\tan(\varphi)$	$(\frac{\pi}{2})\left\lvert\frac{\frac{12\epsilon^2}{(1-\epsilon^2)^{3/2}}-(2a_4-\frac{\epsilon^2+a_4(2-3\epsilon^2)}{(1-\epsilon^2)^{3/2}})a_1(\overline{Re})^{a_2}}{\frac{24\epsilon^3}{(1-\epsilon^2)^2}+(\frac{(1-\epsilon)^{a_2-2}+(1+\epsilon)^{a_2-2}}{(a_2-1)}+\frac{(1-\epsilon)^{a_2-2}-(1+\epsilon)^{a_2-2}}{(a_2-2)(a_2-1)\epsilon})a_1(\overline{Re})^{a_2}}\right\rvert$

Table A2
Analytical stiffness and damping coefficients for turbulent long bearings.

	Turbulent long bearing coefficients (Gümbel boundary condition)
$\bar{k}_{rr}$	$\frac{-\pi}{\epsilon^2(\epsilon^2-1)^2(\epsilon^2((3\hat{a}_3-1)H-12)-2(H+12))^2}\left(\begin{array}{c}3\hat{a}_3^3H^3(5\epsilon^2-3)\epsilon^5-2\hat{a}_3^2H^2(M+12)\\(8\epsilon^4+7\epsilon^2-6)\epsilon^3+\hat{a}_3H(\epsilon^2-1)^2\tanh^{-1}(\epsilon)\\(H(-3\hat{a}_3\epsilon^2+\epsilon^2+2)+12(\epsilon^2+2)+\hat{a}_3H(H+12)^2\\(7\epsilon^6+11\epsilon^4+4\epsilon^2-4)\epsilon-2(H+12)^3(\epsilon^4+2)\epsilon^3)^2\end{array}\right)$
$\bar{k}_{rt}$	$-\frac{\pi^2(\hat{a}_3^2H^2\epsilon^2(-3(1-\epsilon^2)^{1/2}-2\epsilon^2+3)-\hat{a}_3H(H+12)(-(1-\epsilon^2)^{1/2}(\epsilon^2+2)+2)+(H+12)^2\epsilon^2)}{2\epsilon^2\sqrt{1-\epsilon^2}(\epsilon^2((3\hat{a}_3-1)H-12)-2(H+12))}$
$\bar{k}_{tr}$	$\frac{\pi^2}{2(1-\epsilon^2)^{3/2}(\epsilon^3((3\hat{a}_3-1)H-12)-2C(H+12)\epsilon)^2}\left(\begin{array}{c}3\hat{a}_3^3H^3\epsilon^4(3\sqrt{\frac{1+\epsilon}{1-\epsilon}}((\epsilon-2)\epsilon^2+1)+4\epsilon^2-3)\\-3\hat{a}_3^2H^2(H+12)\epsilon^2(2\sqrt{\frac{1+\epsilon}{1-\epsilon}}(\epsilon-1)((\epsilon-1)\epsilon-1)(\epsilon^2+2)+4\epsilon^4+3\epsilon^2-4)\\+\hat{a}_3H(H+12)^2(\sqrt{\frac{1+\epsilon}{1-\epsilon}}(\epsilon^2+2)^2((\epsilon-2)\epsilon^2+1)+6\epsilon^6+5\epsilon^4+2\epsilon^2-4)\\-(H+12)^3(2\epsilon^4-\epsilon^2+2)\epsilon^2\end{array}\right)$
$\bar{k}_{tt}$	$-\frac{\pi(\hat{a}_3^2H^2(2\epsilon^2-3)\epsilon^3-\hat{a}_3H(\epsilon^2-1)\tanh^{-1}(\epsilon)(\epsilon^2((3\hat{a}_3-1)H-12)-2(H+12))+2\hat{a}_3H(H+12)\epsilon-(H+12)^2\epsilon^3)}{\epsilon^2(\epsilon^2-1)(\epsilon^2((3\hat{a}_3-1)H-12)-2(H+12))}$
$\bar{c}_{rr}$	$\frac{-\pi}{2\epsilon^2(1-\epsilon^2)^{3/2}(\pi\epsilon^2((3\hat{a}_3-1)H-12)-2\pi(H+12))}\left(\begin{array}{c}\hat{a}_3^2H^2\epsilon^2(\pi^2(6(1-\epsilon^2)^{3/2}+9\epsilon^2-6)-16\epsilon^4)\\-2\hat{a}_3H(H+12)(\pi^2((1-\epsilon^2)^{3/2}(\epsilon^2+2)+3\epsilon^4+2\epsilon^2-2)\\-16\epsilon^4)+(H+12)^2(\pi^2(\epsilon^2+2)-16)\epsilon^2\end{array}\right)$
$\bar{c}_{rt}$	$-\frac{2\pi(\hat{a}_3^2H^2(3-2\epsilon^2)\epsilon^3+\hat{a}_3H(\epsilon^2-1)\tanh^{-1}(\epsilon)(\epsilon^2((3\hat{a}_3-1)H-12)-2(H+12))-2\hat{a}_3H(H+12)\epsilon+(H+12)^2\epsilon^3)}{\epsilon^2(\epsilon^2-1)(\epsilon^2((3\hat{a}_3-1)H-12)-2(H+12))}$
$\bar{c}_{tr}$	$-\frac{2\pi(\hat{a}_3^2H^2(3-2\epsilon^2)\epsilon^3+\hat{a}_3H(\epsilon^2-1)\tanh^{-1}(\epsilon)(\epsilon^2((3\hat{a}_3-1)H-12)-2(H+12))-2\hat{a}_3H(H+12)\epsilon+(H+12)^2\epsilon^3)}{\epsilon^2(\epsilon^2-1)(\epsilon^2((3\hat{a}_3-1)H-12)-2(H+12))}$
$\bar{c}_{tt}$	$-\frac{\pi^2(\hat{a}_3^2H^2\epsilon^2(-3(1-\epsilon^2)^{1/2}-2\epsilon^2+3)-\hat{a}_3H(H+12)(-(1-\epsilon^2)^{1/2}(\epsilon^2+2)+2)+(H+12)^2\epsilon^2)}{\epsilon^2\sqrt{1-\epsilon^2}(\epsilon^2((3\hat{a}_3-1)H-12)-2(H+12))}$
S	$\frac{1}{\sqrt{(\frac{\pi(\hat{a}_3^2H^2(2\epsilon^2-3)\epsilon^2+2\hat{a}_3H(H+12)-(H+12)^2\epsilon^2)}{(\epsilon^2-1)(\epsilon^2((3\hat{a}_3-1)H-12)-2(H+12))}-\frac{\pi\hat{a}_3H\tanh^{-1}(\epsilon)}{\epsilon})^2-\frac{\pi^4(\hat{a}_3^2H^2\epsilon^2(3\sqrt{\frac{1+\epsilon}{1-\epsilon}}(\epsilon-1)-2\epsilon^2+3)-\hat{a}_3H(H+12)(\sqrt{\frac{1+\epsilon}{1-\epsilon}}(\epsilon-1)(\epsilon^2+2)+2)+(H+12)^2\epsilon^2)^2}{4(\epsilon^2-1)(\epsilon^3(-3\hat{a}_3H+H+12)+2(H+12)\epsilon)^2}}}$
$\tan(\varphi)$	$(\frac{\pi}{2})\left\lvert\frac{\sqrt{1-\epsilon^2}(\hat{a}_3^2H^2\epsilon^2(3\sqrt{\frac{1+\epsilon}{1-\epsilon}}(\epsilon-1)-2\epsilon^2+3)-\hat{a}_3H(H+12)(\sqrt{\frac{1+\epsilon}{1-\epsilon}}(\epsilon-1)(\epsilon^2+2)+2)+(H+12)^2\epsilon^2)}{\hat{a}_3^2H^2(2\epsilon^2-3)\epsilon^3-\hat{a}_3H(\epsilon^2-1)\tanh^{-1}(\epsilon)(\epsilon^2((3\hat{a}_3-1)H-12)-(H+12))+2\hat{a}_3H(H+12)\epsilon-(H+12)^2}\right\rvert$

Appendix B

Stability of a flexible rotor supported on two identical journal bearings

By substituting Eq. (22) into Eq. (21), the following expression may be obtained:

$$\begin{bmatrix} \frac{K_s M\omega_w^2}{M\omega_w^2 - K_s} + 2K_{xx} + 2i\omega_w C_{xx} & 2K_{xy} + 2i\omega_w C_{xy} \\ 2K_{yx} + 2i\omega_w C_{yx} & \frac{K_s M\omega_w^2}{M\omega_w^2 - K_s} + 2K_{yy} + 2i\omega_w C_{yy} \end{bmatrix} \begin{pmatrix} X_1 \\ Y_1 \end{pmatrix} = \begin{pmatrix} 0 \\ 0 \end{pmatrix}. \tag{B1}$$

Using the normalization of $\bar{K}_{ij} = (\pi\,(\frac{C}{R})^3/\mu\omega L)\;K_{ij}$, $\bar{C}_{ij} = (\pi\,(\frac{C}{R})^3/\mu L)\;C_{ij}$, $(i, j{=}x, y)$, $\bar{K}_s = (\pi\,(\frac{C}{R})^3/\mu\omega L)\;K_s$, $(\begin{smallmatrix}\bar{X}_1\\ \bar{Y}_1\end{smallmatrix}) = \frac{1}{C}(\begin{smallmatrix}X_1\\ Y_1\end{smallmatrix})$, $\bar{\omega} = \omega\sqrt{M/K_s}$, $\Omega{=}\omega_w/\omega$, $\gamma = \frac{\bar{K}_s\Omega^2\bar{\omega}^2}{\Omega^2\bar{\omega}^2-1}$, the non-dimensional form of Eq. (A1):

$$\begin{bmatrix} \gamma + 2\bar{K}_{xx} + 2i\Omega\bar{C}_{xx} & 2\bar{K}_{xy} + 2i\Omega\bar{C}_{xy} \\ 2\bar{K}_{yx} + 2i\Omega\bar{C}_{yx} & \gamma + 2\bar{K}_{yy} + 2i\Omega\bar{C}_{yy} \end{bmatrix} \begin{pmatrix} \bar{X}_1 \\ \bar{Y}_1 \end{pmatrix} = \begin{pmatrix} 0 \\ 0 \end{pmatrix}. \tag{B2}$$

The condition of non-trivial (non-zero) solution requires that the determinant of the characteristic matrix to be set to zero. By setting the imaginary part of the determinant of Eq. (B2) to zero:

$$\gamma = \frac{2\left(\bar{K}_{xy}\bar{C}_{yx} + \bar{K}_{yx}\bar{C}_{xy} - \bar{K}_{yy}\bar{C}_{xx} - \bar{K}_{xx}\bar{C}_{yy}\right)}{\bar{C}_{xx} + \bar{C}_{yy}} \tag{B3}$$

By setting the real part of the determinant of Eq. (B2) to zero, the whirl frequency ratio can be calculated as:

$$\Omega^2 = \frac{\gamma^2 + 2\left(\bar{K}_{xx} + \bar{K}_{yy}\right)\gamma + 4\left(\bar{K}_{xx}K_{yy} - \bar{K}_{xy}\bar{K}_{yx}\right)}{4\left(\bar{C}_{xx}\bar{C}_{yy} - \bar{C}_{xy}\bar{C}_{yx}\right)} \tag{B4}$$

Using the definition of non-dimensional parameter γ, the instability threshold speed can be found as:

$$\bar{\omega}_s^2 = \frac{\gamma}{\Omega^2\left(\gamma - \bar{K}_s\right)}, \tag{B5}$$

where $\bar{K}_s = (\pi\,(\frac{C}{R})^3/\mu\omega L)K_s = \frac{1}{S}\frac{C}{W}\frac{K_s}{}$.

References

[1] J.M. Vance, B. Murphy, F. Zeidan, Machinery Vibration and Rotordynamics, Wiley Online Library, 2010.
[2] J.M. Vance, Rotordynamics of Turbomachinery, Wiley-Interscience, 1988.
[3] F.K. Choy, M.J. Braun, Y. Hu, Nonlinear effects in a plain journal bearing: Part 1—analytical study, J. Tribol. 113 (1991) 555–561.
[4] L.S. Andréas, O. De Santiago, Identification of journal bearing force coefficients under high dynamic loading centered static operation, Tribol. Trans. 48 (2005) 9–17.
[5] V. Meruane, R. Pascual, Identification of nonlinear dynamic coefficients in plain journal bearings, Tribol. Int. 41 (2008) 743–754.
[6] S. Muzakkir, H. Hirani, G. Thakre, Lubricant for heavily loaded slow-speed journal bearing, Tribol. Trans. 56 (2013) 1060–1068.
[7] M. Lahmar, S. Ellagoune, B. Bou-Saïd, Elastohydrodynamic lubrication analysis of a compliant journal bearing considering static and dynamic deformations of the bearing liner, Tribol. Trans. 53 (2010) 349–368.
[8] U.P. Singh, R.S. Gupta, V.K. Kapur, On the steady performance of hydrostatic thrust bearing: rabinowitsch fluid model, Tribol. Trans. 54 (2011) 723–729.
[9] A.Z. Szeri, Fluid Film Lubrication, vol. 2, Cambridge University Press, Cambridge, 2011.
[10] H. Hashimoto, S. Wada, An influence of inertia forces on stability of turbulent journal bearings, Bull. JSME 25 (1982) 653–662.
[11] H. Hashimoto, S. Wada, J.-I. Ito, An application of short bearing theory to dynamic characteristic problems of turbulent journal bearings, J. Tribol. 109 (1987) 307–314.
[12] J. Wang, M. Khonsari, Application of Hopf bifurcation theory to rotor-bearing systems with consideration of turbulent effects, Tribol. Int. 39 (2006) 701–714.
[13] C.-W. Chang-Jian, C.o.-K. Chen, Bifurcation and chaos of a flexible rotor supported by turbulent journal bearings with non-linear suspension, Proc. Inst. Mech. Eng., Part J: J. Eng. Tribol. 220 (2006) 549–561.
[14] C.-W. Chang-Jian, C.-K. Chen, Bifurcation and chaos analysis of a flexible rotor supported by turbulent long journal bearings, Chaos Solitons Fractals 34 (2007) 1160–1179.
[15] J. Wang, M. Khonsari, Bifurcation analysis of a flexible rotor supported by two fluid-film journal bearings, J. Tribol. 128 (2006) 594–603.
[16] J.W. Lund, Self-excited stationary whirl orbits of a journal in a sleeve bearing, Rensselaer Polytechnic Institute, Ph.D. Thesis, 1966.
[17] R. DiPrima, A note on the stability of flow in loaded journal bearings, ASLE Trans. 6 (1963) 249–253.
[18] C. Taylor, D. Dowson, Turbulent lubrication theory—application to design, J. Lubr. Technol. 96 (1974) 36–46.
[19] V. Constantinescu, On turbulent lubrication, Proc. Inst. Mech. Eng. 173 (1959) 881–900.
[20] H. Elrod, C. Ng, A theory for turbulent fluid films and its application to bearings, J. Lubr. Technol. 89 (1967) 346–362.
[21] J. Frene, D. Nicolas, B. Degueurce, D. Berthe, M. Godet, Hydrodynamic Lubrication: Bearings and Thrust Bearings, 33, Elsevier, 1997.
[22] J. Durany, J. Pereira-Pérez, F. Varas, About the Constantinescu turbulent model in hydrodynamic lubrication: a comparison with 3-D LES models, Tribol. Int. 83 (2015) 33–41.
[23] J.W. Lund, Self-Excited, Stationary Whirl Orbits of a Journal in a Sleeve Bearing, Rensselaer Polytechnic Institute, 1966.
[24] A.Z. Szeri, Fluid Film Lubrication, Cambridge University Press, 2010.
[25] G. Capone, M. Russo, R. Russo, Dynamic characteristics and stability of a journal bearing in a non-laminar lubrication regime, Tribol. Int. 20 (1987) 255–260.
[26] A. Raimondi, A. Szeri, Journal and thrust bearings, CRC Handbook of Lubrication: Theory and Practice of Tribology, Volume II: Theory and Design, 2, 1988, p. p. 413.

[27] P. Hollis, D. Taylor, Hopf bifurcation to limit cycles in fluid film bearings, J. Tribol. 108 (1986) 184–189.
[28] B.D. Hassard, N.D. Kazarinoff, Y.-H. Wan, Theory and Applications of Hopf Bifurcation, 41, CUP Archive, 1981.
[29] C. Myers, Bifurcation theory applied to oil whirl in plain cylindrical journal bearings, J. Appl. Mech. 51 (1984) 244–250.
[30] M. Khonsari, Y. Chang, Stability boundary of non-linear orbits within clearance circle of journal bearings, J. Vib. Acoust. 115 (1993) 303–307.
[31] J. Wang, M. Khonsari, Prediction of the stability envelope of rotor-bearing system, J. Vib. Acoust. 128 (2006) 197–202.